Toward Zero-Strain Mixed Conductors: Anomalously Low Redox Coefficients of Chemical Expansion in Praseodymium-Oxide Perovskites

*Lawrence O. Anderson[1,2], Adrian Xiao Bin Yong[1,2], Elif Ertekin[2,3], and Nicola H. Perry[1,2]**

1. Department of Materials Science & Engineering, University of Illinois at Urbana-Champaign

2. Materials Research Laboratory, University of Illinois at Urbana-Champaign

3. Department of Mechanical Science & Engineering, University of Illinois at Urbana-Champaign

104 S. Goodwin Ave, Urbana IL. 61801, U.S.A.

* Corresponding author: nhperry@illinois.edu

Keywords: Chemical expansion, zero-strain, band structure, redox, perovskite

ABSTRACT

Zero-strain materials are desired for high chemo-mechanical stability in energy conversion/storage devices, where operational stoichiometry changes can cause large chemical stresses. Here, we demonstrate near-zero redox coefficients of chemical expansion (CCEs) for mixed- and triple-conducting Pr-oxide perovskites. $PrGa_{0.9}Mg_{0.1}O_{3-\delta}$ (PGM) and $BaPr_{0.9}Y_{0.1}O_{3-\delta}$ (BPY), having Pr on the A- and B-site respectively, were synthesized and characterized with

in situ high temperature, variable atmosphere X-ray diffraction, dilatometry, and thermogravimetric analysis, to obtain isothermal stoichiometry changes, chemical strains, and CCEs. Despite empirical model predictions of smaller CCEs for Pr on the A-site, both compositions yielded unprecedented low average CCEs (0.004-0.011), 2-5x lower than the lowest reported perovskite redox CCEs. Simple empirical models assume pseudo-cubic structures and full charge localization on multivalent cations, like Pr. To evaluate actual charge distribution, in situ impedance spectroscopy and density functional theory calculations were performed. Results indicate the anomalously low CCEs in these compositions likely derive from a combination of decreased crystal symmetry (vs. cubic), partial charge delocalization through hybridization of Pr-*4f* and O-*2p* orbitals, and redox/multivalence on O rather than just Pr (with or without hybridization). On this basis, we suggest band structure design principles for near-zero redox-strain perovskites, highlighting the benefit of locating holes partially or fully on oxygen.

1. INTRODUCTION

Changes in composition are almost always associated with a strain. This chemically-induced strain is known as a prominent mode of mechanical degradation in solid-state electrochemical devices including fuel cells[1,2], electrolysis cells[1,2], gas separation membranes[3,4], electrochemical generators, and batteries[5–7]. Where local materials' compositions may change during fabrication, start/stop cycles, and/or operation, and where multilayer or constrained device designs give rise to enhanced stresses, failure including cracking and delamination can result. In this context, materials with low chemical expansion are desirable, and the search for "zero-strain" electrodes is a research thrust attracting broader attention, having initiated in the batteries field[8]. On the other hand, a lesser-known emerging application is that of chemically-driven actuators[9], e.g., for use in extreme conditions. In this case the chemical strain is a beneficial property, where larger strains enable more significant

displacement. Similarly, recently developed characterization techniques[10–12] leverage the stoichiometry-strain coupling of this class of materials in order to study ion/defect concentrations and kinetics; again, here a large chemically-induced lattice dilation or contraction is desirable for accurate detection of stoichiometry and stoichiometry changes.

In ionically bonded materials, the chemical strain cannot simply be interpreted in terms of the difference in effective radii of the host and replacement ions (if known). Rather, ion loss, insertion, or aliovalent substitution cause changes in charged point defect concentrations, in order to maintain overall charge neutrality. Even isovalent substitution can alter the formation energies of point defects and therefore their concentrations under equilibrium conditions. Ionic point defects, including vacancies, have associated effective volumes[13–15] and shapes[16] and therefore play a critical role in the magnitude of macroscopic chemical strains. Furthermore, electronic point defects, including electrons and holes, can exhibit a range of degrees of localization, with varying resulting lattice distortions[17]. Taken together, these point defect chemical effects result in chemical strains that may elude intuition and description with simple models. Nonetheless, if it could be achieved, identification of underlying design principles linking multiscale structural features (electronic structure, crystal structure, microstructure, etc.) with macroscopic chemical expansion behavior would have enormous technological consequences, given the ubiquity of chemo-mechanical coupling across solid state ionics applications.

This paper focuses on perovskite-structured mixed ionic and electronic conductors (MIECs) that undergo strain relating to changes in their oxygen stoichiometry. The relationship between stoichiometry changes and strain is often described quantitatively by the tensor quantity of "chemical expansivity"[2] or its linearized scalar version, coefficient of chemical expansion (CCE), analogous to a coefficient of thermal expansion. The CCE typically refers to "stoichiometric" chemical expansion, rather than "phase-change" expansion, i.e., composition

changes giving rise to monotonic and continuous lattice parameter shifts in a single-phase material[5]. A CCE value is beneficial for enabling comparison between materials because it normalizes the chemical strain to the stoichiometry change. In this work, the coefficient of chemical expansion (α_c) due to oxygen loss is expressed in terms of isothermal chemical strain (ε_c) and isothermal change in oxygen non-stoichiometry ($\Delta\delta$) by Equation 1.

$$\alpha_c = \frac{\Delta L/L}{\Delta[v_O^{\cdot\cdot}]/_{[ABO_3]}} = \frac{\varepsilon_c}{\Delta\delta} \quad (1)$$

Note that this unitless form of the CCE is widely used but best only applied for comparison among perovskites (or compositions with the same nominal formula units). For more generalizable comparisons among materials with different formula units, a CCE (with units of cm^3) defined as strain per change in volumetric defect concentration may be used instead[18]. Experimentally, changes in oxygen non-stoichiometry can be introduced through changes in the partial pressure of oxygen (pO_2) in the local gas environment. As the local pO_2 decreases, e.g. by increasing the Ar: O_2 ratio, oxygen evolves from the solid phase into the gas if the temperature is high enough or the time is long enough to overcome the energetic and kinetic barriers of diffusion and surface exchange. A typical example of the oxygen evolution reaction for a metal oxide (M_xO_y) is shown in Equation 2a, where O_o^x is lattice oxygen, $v_o^{\cdot\cdot}$ is a lattice oxygen vacancy, and e' is an electron.

$$O_o^x \rightarrow v_o^{\cdot\cdot} + \frac{1}{2}O_2 + 2e' \quad (2a)$$

In prior work on chemical expansion, the electrons released from the oxygen site were assumed to be localized on the neighboring multivalent cations[15]. This reduction of two cations to a lower valence state results in an overall expansion of the crystal lattice and bulk material, even though the generated oxygen vacancy may be slightly smaller or of a similar size to the previously occupied oxygen site[14,15]. Although this assumption of charge localization at the cations holds for some strongly ionic systems, the electrons can in principle also be delocalized to different

degrees. Further, many of the perovskites are p-type in mildly oxidizing conditions, as in the present study. It is thus illustrative to represent the oxygen evolution reaction in terms of filling holes rather than generating electrons:

$$O_o^x + 2h^{\cdot} \rightarrow v_o^{\cdot\cdot} + \frac{1}{2}O_2 \quad (2b)$$

Analogous to Equation 2a, Equation 2b presents the holes as free carriers; however, holes may also be located on anions or on cations, or covalently shared between oxygen and metal.

Previous research by our group and others has begun to investigate structural and chemical factors that play a key role in determining the magnitude of the CCEs in this class. To date, crystal chemical factors including charge localization[17,19,20], anisotropic lattice expansion[21–23], spin state of magnetic cations[24], and defect ordering[23,25,26] have been suggested as important variables for tailoring the CCE, but the generalizability of these findings to various compositions has not yet been tested. In the present work, we continue to pursue design principles for tailored chemo-mechanical coupling by examining the CCEs of two previously chemo-mechanically unstudied perovskite compositions, $PrGa_{0.9}Mg_{0.1}O_{3-\delta}$ (PGM) and $BaPr_{0.9}Y_{0.1}O_{3-\delta}$ (BPY) by systematic experimental and computational approaches.

From a fundamental scientific standpoint, we chose these compositions for two reasons: 1) We wished to examine for the first time the impact of placing the multivalent cation (expected to be Pr in this case) on the A- vs. B-site of the perovskite. Various models have been presented to predict the lattice parameters of perovskite oxides based on their composition and ionic radii[15,27–29], primarily with the goal of describing lattice parameters as a function of doping. The empirical model by Marrocchelli et al.[15] is:

$$a = 0.577(r_A + r_X) + 1.437(r_B + r_X) - 0.609 \quad (3)$$

where a is the pseudocubic lattice parameter (in Å) and r_A, r_B, and r_X are the A-site, B-site, and anion site ionic radii (in Å), respectively. The numerical coefficients in this equation indicate

that a change in radius at the B-site would have a significantly larger effect on the lattice parameter than an equal change at the A-site. 2) We wished to examine the CCEs of compositions with an *f*-electron multivalent cation, in contrast to the *d*-electron transition metal oxide perovskites that have been experimentally measured to-date in the literature. One prior computational study found that in a different *f*-electron system, CeO_{2-x}, the degree of charge localization, as manipulated via the U parameter in density functional theory (DFT) simulations, had a significant effect on the CCE – modifying it by up to 70%. While we have tested the role of charge localization experimentally in other perovskite systems, we have observed relatively modest effects (~10-40% change in CCE) for *d*-electron multivalent cations[19,20].

From an applied standpoint, the BPY and PGM compositions in the present work fit into the first class of applications noted in the first paragraph; PGM is expected to be a mixed ionic/electronic conductor[30] that might be chemically compatible as a Sr-free electrode with the fast oxygen-ion-conducting electrolyte $La_{1-x}Sr_xGa_{1-y}Mg_yO_{3-\delta}$ (LSGM) in solid oxide fuel/electrolysis cells, and BPY is a triple (protonic, oxide ionic, and electronic) conductor[31–33] of potential interest for electrodes of protonic ceramic fuel/electrolysis cells in CO_2-poor conditions, although we study it under dry conditions in this work. As noted above, in these uses, low CCEs are desirable to mitigate mechanical degradation.

Through application of complex oxide synthesis, *in situ* dilatometry, thermogravimetric analysis (TGA), and high temperature X-ray diffraction, combined with DFT simulations, we find that both compositions exhibit unusually low CCEs for oxygen stoichiometry changes. The CCEs are significantly lower than any previously reported experimentally for MIEC perovskites. We find that the effect of A- vs. B-site placement of the multivalent cation is insufficient to explain the low CCEs of both compositions. The simple empirical model predictions regarding Pr placement do not agree with experimental CCEs, although the empirically predicted trend agrees with DFT when the parameter U is selected so that the holes

formed by acceptor doping localize on Pr. More importantly, reduced crystal symmetry, redox on oxygen (multivalent O), and partial delocalization of holes, further examined through *in situ* impedance spectroscopy, appear to be more pronounced factors in lowering the CCEs. Specifically, we propose that two cases can lead to ultra-low CCEs: the filling of holes located on oxygen rather than on (Pr) cations, and the filling of somewhat delocalized holes achieved by hybridization of the metal (Pr) *f* and oxygen *p* orbitals, given the ability of B-site Pr to form covalent bonds. This work therefore demonstrates that 1) simple empirical models based on ionic radii and a limited database of compositions do not yet predict CCEs or their trends with sufficient precision, and 2) extremely low CCEs can be achieved in perovskites. Use of these Pr-bearing compositions in devices or other compositions derived from the design principles highlighted in this work can dramatically mitigate chemo-mechanical failure.

2. METHODS

2.1. Experimental Methods: A modified Pechini synthesis route was used to fabricate both BPY and PGM. First, stoichiometric amounts of metal nitrates $Pr(NO_3)_3$ (99.9%, Alfa Aesar), $Mg(NO_3)_2$ (99.999%, Acros Organics), $Ga(NO_3)_3$ (99.9998%, Acros Organics), $Ba(NO_3)_2$ (99.999%, Alfa Aesar), and/or $Y(NO_3)_3$ (99.99%, Alfa Aesar) were added to deionized water. Most nitrates readily dissolved, but barium nitrate required raising the pH to 6 to form a clear solution. The quantity of citric acid (CA) and ethylene glycol (EG) needed to form a stable polymer network is based on the molar quantity of total transition metals (TM) in solution. Citric acid (Fisher chemical) was added to the solution in the molar ratio 4:1 CA:TM and was stirred continuously at 60° C for at least 30 minutes to allow sufficient time for the chelation reactions. After balancing the pH with ammonia to nearly 6, ethylene glycol (Fisher chemical) was added in the molar ratio 3:1 EG:CA and the solution was heated to 90° C. The solution was stirred under heat until a very viscous gel was formed, and the gel was placed in a furnace at 200° C to evaporate the excess water. The resulting dry gel was calcined at 800° C for 6 hours

to remove the organics, leaving a fine powder behind. The powder was ground in a zirconia mortar and pestle, uniaxially pressed at 125 MPa, sintered at 1400° C (PGM) or 1500° C (BPY) for 10 hours to give highly dense pellets, and finally cut into a bar (dilatometry) using a low-speed saw (ALLIED TechCut 4) with diamond blade or ground into a coarse powder (TGA).

Phase purity was determined by X-ray diffraction with the Bruker D8 Advance (Model # D8 Advance A25) using Cu kα radiation with line focus, 60 mm Göbbel mirror and 0.2 mm divergence slit primary optics, and Dectris Eiger2R_500K detector. Scans were taken using 0.01° 2θ step size, 0.10 seconds/step, in the 10-100° 2θ range. The microstructure was viewed with the JEOL 7000 SEM, seen in Figure 1. Samples were prepared for SEM using ALLIED Diamond Lapping Film by dry polishing with gradually increasing fineness from 35 micron to 0.1 micron films, followed by thermal etching at 1200-1300° C for one hour to better visualize grain boundaries. Images were then taken using the secondary electron detector with a working distance of 10.0 mm and 10.0 kV accelerating voltage.

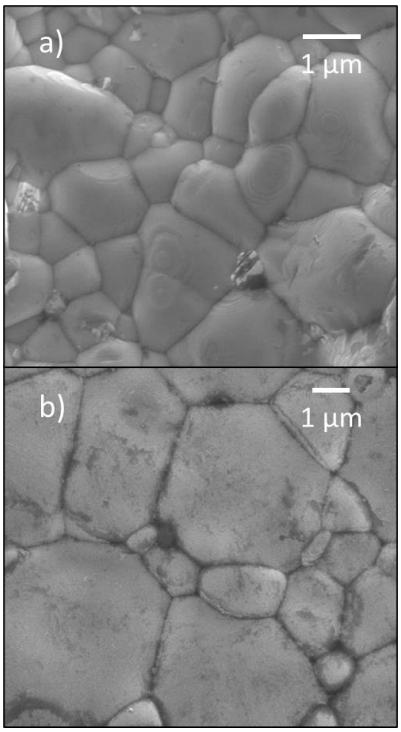

Figure 1. SEM images of polished and thermally-etched surfaces of dense pellets of BPY (a) and PGM (b).

In situ, high temperature X-ray diffraction (HTXRD) was conducted using the Anton Paar HTK 1200N Non-ambient stage in the Bruker D8 described above. To set up the HTXRD experiment, the stage was centered, and the Z height was corrected with the 1/2 intensity cutoff calculation using the 0.1 mm frame reduction Soller slit. A thermocouple in contact with the bottom of the sample stage monitored the sample temperature. The scan parameters were the same as those listed above, but the scan time was increased to 0.15 seconds/step, and the scan range was changed to 20-100° 2θ. The gases used for the sample environment were either UHP argon or UHP oxygen, and the flow rate was 40 sccm for all runs. Each sample was ground to a fine powder with mortar and pestle to give a good distribution of grain orientations while avoiding small crystal sizes that would cause peak broadening. Particle size reduction using high energy ball mills can give crystal sizes that are too small[34,35]. The samples were mounted, and the gas environment was introduced. The samples were then heated at 30° C min^{-1} to 900° C and held for 3 hours before taking a scan from 20-100° 2θ. The sample was then ramped down to 700° C, held for 3 hours, and scanned again. At each isothermal hold, repeated scans were also taken over peaks at 81.5° 2θ (BPY hkl: 321) and 58° 2θ (PGM hkl: 132, 024, 204, 312) every 30 minutes to determine the degree of equilibration before the final scan.

Rietveld refinements were performed in TOPAS (Bruker AXS, Version 6), initiated from previously determined structure files (PGM *Pbnm*: ICSD# 153163[36], BPY $R\bar{3}c$: ICSD# 163758[31], BPY $Pm\bar{3}m$: ICSD# 163759[31]). After fitting the background using 5th order Chebychev polynomials, Lattice parameters were refined first, and additional parameters were included into the refinement in following order: sample displacement correction, microstrain, and Pitschke surface roughness correction.

Dilatometry (Linseis dual push-rod dilatometer L75HD 1600 C) and TGA (in-house assembled[37]) measurements were taken in precise gas mixtures of $Ar/N_2/O_2$, determined by mass-flow controllers, to give the desired pO_2 under isothermal holds at 700, 800, and 900° C.

Reversibility in the measured strain and mass change was checked by returning to previous pO_2 values at each isothermal hold. Both PGM and BPY exhibited unprecedented low strain (compared to other mixed conducting perovskites studied by our group), so the accuracy of the dilatometer was verified using a $SrTi_{0.65}Fe_{0.35}O_3$ (STF35) reference that has been characterized thoroughly for both thermal and chemical expansion in previous work[20,38,39]. There was excellent agreement in STF35 strain between our instrument and literature values, indicating high accuracy for our dilatometric instrument and the supplied pO_2. We further calibrated the dilatometer response in different gas atmospheres and temperatures with reference runs on standard compositions. To obtain the most accurate pO_2 measurements, the pO_2 was measured close to the samples in the TGA using a home-built zirconia Nernst sensor.

Two-point AC impedance spectroscopy measurements (Ametek/Solartron ModulabXM ECS impedance analyzer with femtoammeter and potentiostat attachments) were performed on dense bars of both compositions using a custom-built, high-temperature sample holder in a tube furnace (Thermo Scientific Lindberg/Blue M). The custom sample holder incorporated shielded electrical leads, and measurements were taken under controlled gas atmosphere and temperature to evaluate the electrical behavior and, indirectly, the localization of charge carriers. The impedance measurements were taken with 300 mV voltage amplitude from 1 MHz to 1 Hz. Sample areas were 0.09 cm^2 (BPY) and 0.20 cm^2 (PGM), and sample lengths were 0.70 cm (BPY) and 0.38 cm (PGM). Porous silver current collectors covered opposing sides of each sample by adhering silver paint in a thin layer, and platinum wires were adhered to the current collecting layer with silver paste. The samples were first heated in dry gas (21% O_2, 79% N_2) to 300^o C and held for over 4 hours to allow time for any water to be purged from the tube and the sample, and any oxygen vacancy concentration equilibration, that could influence the impedance results. The samples were then taken to 400^o C for the first impedance measurement. The subsequent measurements were taken at successively cooler temperature points after an

isothermal hold of at least 30 minutes. The impedance spectra were analyzed by equivalent circuit fitting with a R(RQ) circuit (Boukamp notation). A geometric correction according to the dimensions of the pellets was performed to calculate measured conductivity from the measured resistance.

2.2. Computational Methods: DFT calculations were performed using the Vienna Ab initio Simulation Package (VASP)[40–43], with the projector augmented-wave (PAW) method[44,45]. The Pr ($5s^2$ $5p^6$ $5d^1$ $4f^2$ $6s^2$), Ga ($3d^{10}$ $4s^2$ $4p^1$), Mg ($3s^2$), Ba ($5s^2$ $5p^6$ $6s^2$), Y ($4s^2$ $4p^6$ $4d^2$ $5s^1$), and O ($2s^2$ $2p^6$) electrons were treated as valence electrons in the pseudopotentials. The generalized gradient approximation (GGA) with the Perdew-Burke-Ernzerhof (PBE) exchange-correlation functional[46] was used, and the orbitals were expanded using a plane wave basis with cutoff energy of 520 eV. Calculations for $PrGaO_3$ (space group *Pbnm*) and $BaPrO_3$ (space group $Pm\bar{3}m$) were performed using 2×2×1 and 2×2×4 unit cells respectively, where each supercell has a total of 80 atoms for both materials. Although $BaPrO_3$ undergoes a transition[31] from trigonal $R\bar{3}c$ to cubic $Pm\bar{3}m$ in the experimental temperature range of 700-900 °C, the cubic crystal structure was chosen for simplicity. The Brillouin zone was sampled using a (2×2×2) Monkhorst-Pack *k*-point grid for both materials. As $BaPrO_3$ is antiferromagnetic at T = 0 K, those calculations were performed with spin-polarization included, and initialized with the *G*-type antiferromagnetic ordering presented by Rosov *et al*.[47]

The DFT+*U* method[48,49], based on Dudarev's approach[50], was used to account for the electron localization of the Pr-*4f* states. Standard DFT functionals typically do not properly describe localized states such as *d* and *f* orbitals[51], but the description is often improved by including a Hubbard *U* term to the Hamiltonian[52–54]. Since the optimal value of the parameter *U* for Pr-*4f* states is not known, calculations were performed scanning between $U = 0$ and $U =$ 10 eV, and the results were found to be highly sensitive to the value of *U* (discussed below). Below, for $PrGaO_3$ we show results for $U = 4$ and $U = 10$ eV, whereas for $BaPrO_3$ we show

results for $U = 0$ and $U = 6$ eV to highlight a range of possible behaviors. For each supercell, two B-site atoms were replaced with acceptor dopants, giving the compositions $PrGa_{0.875}Mg_{0.125}O_3$ and $BaPr_{0.875}Y_{0.125}O_3$. Structural relaxation was performed, allowing the cell shape, cell volume, and atom positions to relax, until the force on each atom was below 0.01 eV $Å^{-1}$. Then, one O vacancy was introduced to each supercell such that the acceptor dopants were ionically compensated, followed by the same structural relaxation. Pseudo-cubic lattice parameters were calculated from the equilibrium volumes, and subsequently used to determine the strain (relative to the doped structures containing no O vacancies, *i.e.* $\delta=0$). Note that the DFT-calculated strains correspond to strains at $T = 0$ K and use a different reference stoichiometry compared to the experimental strains. In all cases the total energies and equilibrium volumes were well converged (within 2 meV/atom and 0.1% respectively) with the k-point grid density and relaxation forces.

Given the large number of possible configurations for distributing the dopant atoms and O vacancy, only two extreme cases were considered: (1) dopant atoms and O vacancy close together forming a dopant-vacancy-dopant chain, and (2) dopant atoms and O vacancy distributed far apart arbitrarily. For PGM, it was found that having the dopants and O vacancy far apart is energetically favorable by at least 0.17 eV; hence, the chemical expansion results will be presented with respect to this arrangement only. For BPY, the opposite was found where it is energetically favorable by at least 0.14 eV for the dopants and O vacancy to be close together, so the results for BPY will be presented for this arrangement only. The VESTA program[55] was used to visualize the structures and generate charge density plots.

The degree of hybridization between the metal cations and oxygen orbitals was studied by performing projected crystal orbital Hamilton populations (pCOHP)[56,57] calculations using the LOBSTER program[58–61]; further details are provided in the supporting information.

2. RESULTS

Phase purity determined by XRD was performed by comparing the scan data to ICSD standards (PGO: ICSD 153163[36], BPY: ICSD 163756[31]). $BaPr_{0.9}Y_{0.1}O_{3-\delta}$ (BPY) had good agreement with all peak positions of the corresponding ICSD file (See Supporting Information, Figure S1), and the $PrGa_{0.9}Mg_{0.1}O_{3-\delta}$ (PGM) peaks were shifted slightly to the left relative to undoped $PrGaO_3$ (Figure S2). Solid solution Mg doping at the concentration used does not result in additional peaks, but a slight shift to lower 2θ values is observed. Lower 2θ corresponds to larger d-spacing, and an increase in the lattice parameters is expected due to the larger size of Mg^{2+} relative to Ga^{3+}.

2.1. Experimental CCE: Isothermal chemical strains were calculated from dilatometry as $\varepsilon=\Delta L/L_0$, and an example of data from dilatometry relating the chemical strains to changes in pO_2 over time can be seen in Figure S3. Average values along each plateau are taken as the chemical strain at a given pO_2. Forward (Ar to O_2) and reverse (O_2 to Ar) strain values are shown in Figure S4a-c, and the difference between forward and reverse measurements is used for error bars in Figure 2, as this was the largest source of error for this measurement. Additional error is included for the more oxidizing conditions due to longer equilibration times. The chemical strains at each pO_2 value are shown in Figure 2 for each temperature measured; here, 1 atm O_2 at each temperature is set to be the 0% strain reference state ($L=L_0$) for both samples (note the reference length L_0 is therefore different for each temperature and composition). As pO_2 decreases, the strains monotonically increase for each condition as oxygen vacancies begin to form, and unsurprisingly the maximum strains relative to 1 atm O_2 occur at the lowest pO_2 tested: Ar near $pO_2 \approx 10^{-4}$ atm. For PGM, the maximum percent chemical strain (%ε) over this pO_2 range is 0.015, 0.007, and 0.005 at 700° C, 800° C, and 900° C, respectively. For BPY, the maximum percent chemical strain over this pO_2 range is 0.016, 0.024, and 0.037 at 700° C, 800° C, and 900° C, respectively. At a given pO_2, BPY shows an increase in the magnitude of the

chemical strain with increasing temperature, while PGM shows a decrease in overall strain with increasing temperature. Thermochemical strains (Figure S5) and the coefficients of thermochemical expansion in O_2 (Table S1) have also been recorded.

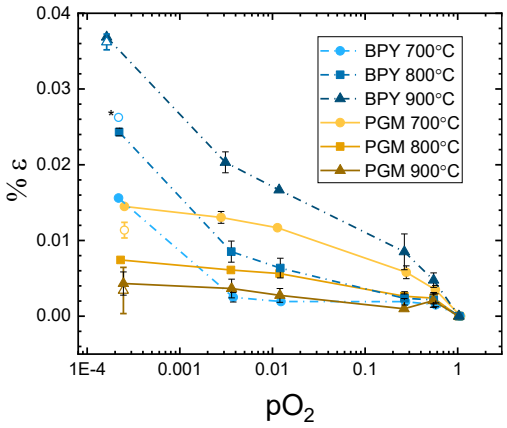

Figure 2. Comparison of the overall chemical expansion measured via dilatometry and HTXRD. Dashed lines represent BPY, and solid lines represent PGM. Temperatures 900°, 800°, and 700° C are shown with triangle, square, and circle symbols, respectively, for both compositions. Open symbols show the HTXRD comparison for the corresponding symbol in the dilatometry data (filled symbols). Strain error bars for HTXRD are calculated from the lattice parameter refinement error, and the error bars for dilatometry represent the deviation from reversibility measurements. Error bars smaller than the symbols are not shown. Reference length is pure O_2 at each temperature.
*this data point has large refinement errors due to a lack of equilibration at this measurement step.

As with the dilatometry data, time-dependent TGA data are shown in Figure S6. Figure 3 shows the change in stoichiometry calculated from averaging the plateaus of TGA data for each material; the $\Delta\delta$ values are given relative to the stoichiometry at 700° C in pure O_2. Instrument noise was found to be the largest source of error for these measurements, and the standard deviation of the noise at each temperature is shown as error bars for all stoichiometry data. The change in oxygen non-stoichiometry for BPY shows a similar trend as the strain, where higher values of $\Delta\delta$ occur with increasing temperature and correlate to the larger strain values in Figure 2. For BPY, the maximum $\Delta\delta$ (in Ar) is 0.020, 0.025, and 0.034 at 700° C, 800° C, and 900° C, respectively. PGM does not show a significant temperature dependent

stoichiometry change, and the values plateau at $\Delta\delta \sim 0.013$-0.015 under reducing conditions for all temperatures, relative to the reference state at 700° C in O_2.

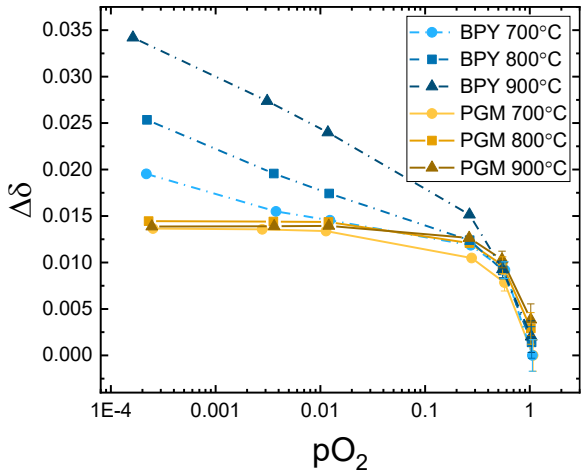

Figure 3. Change in stoichiometry ($\Delta\delta$) vs experimental pO_2. Dashed lines represent BPY, and solid lines represent PGM. Temperatures 900°, 800°, and 700° C are shown with triangle, square, and circle symbols, respectively, for both compositions. Error bars smaller than data symbols are not shown. Reference stoichiometry is at 1 atm O_2 at 700° C.

Figure 4 and 5 show the relationship between the measured strain and change in stoichiometry for PGM and BPY, respectively. The reference point is 700° C in O_2 for both strain and nonstoichiometry (thermochemical strain at 800° and 900° C is included, but isothermal data represent pure chemical strain). Figure S7 and S8 show the data in Figure 4 and 5 using alternative reference points of 1 atm O_2 at each temperature, which elucidates the nonlinear chemical expansion for both compositions. Perovskite materials often exhibit a linear relationship between these properties over limited experimentally reported ranges of $\Delta\delta$, and the slope is taken as the coefficient of chemical expansion (CCE); see Eq. 1. In contrast, both PGM and BPY exhibit nonlinear behavior that may be the result of two superimposed linear regions that each become dominant within different pO_2 ranges. Following this interpretation, limiting slopes (CCE values) were determined in the high and low $\Delta\delta$ regions that individually

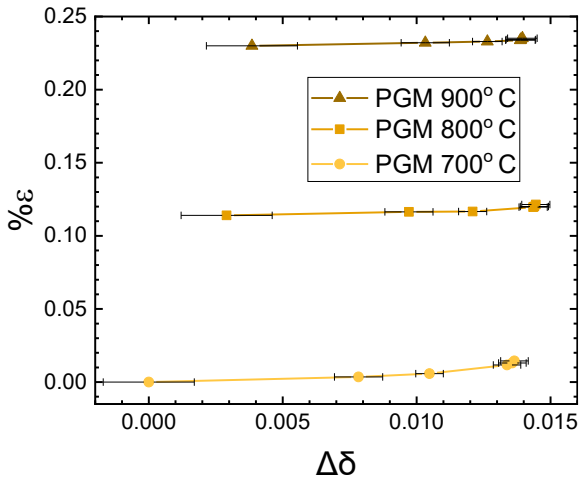

Figure 4. Chemical strain (%ε) vs. change in stoichiometry (Δδ) for PGM. Temperatures 900°, 800°, and 700° C are shown with triangle, square, and circle symbols, respectively. The strain error bars are smaller than the data points for all data shown. Stoichiometry error bars represent instrument noise and slow equilibration errors at each temperature. Error bars smaller than the symbols are not shown. Reference condition for strain and stoichiometry is 1 atm O_2 at 700° C.

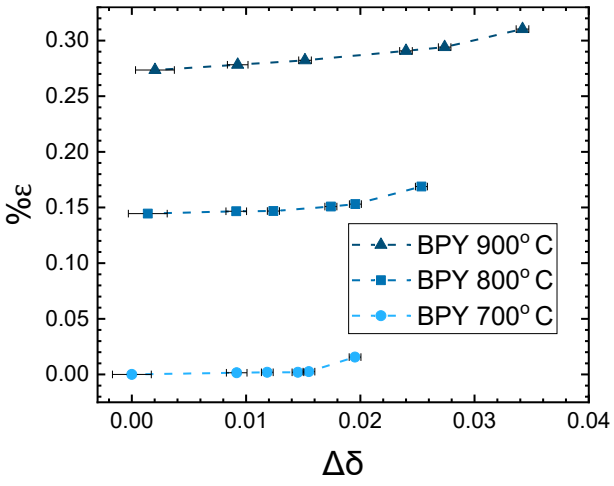

Figure 5. Chemical strain (%ε) vs. change in stoichiometry (Δδ) for BPY. Temperatures 900°, 800°, and 700° C are shown with triangle, square, and circle symbols, respectively. The strain error bars are smaller than the data points for all data shown. Stoichiometry error bars represent instrument noise and slow equilibration errors at each temperature. Error bars smaller than the symbols are not shown. Reference condition for length and stoichiometry is 1 atm O_2 at 700° C.

appear nearly linear. A comparison between this work and representative perovskite data from literature is shown in Figure 6, where all previously reported materials (to the authors' knowledge) fall within the shaded region. Among the selected perovskites shown in Figure 6, compositions exhibiting the highest and the lowest CCEs (for perovskites) reported in literature,

$La_{0.3}Sr_{0.7}Fe_{0.6}Ga_{0.4}O_3$ and $La_{0.3}Sr_{0.7}FeO_3$, respectively, are included[20,62,63]. When scaled to typical perovskite expansion values, the data from the present work appear more linear, so average values of CCE are also calculated, and the CCE summary is presented in Table 1.

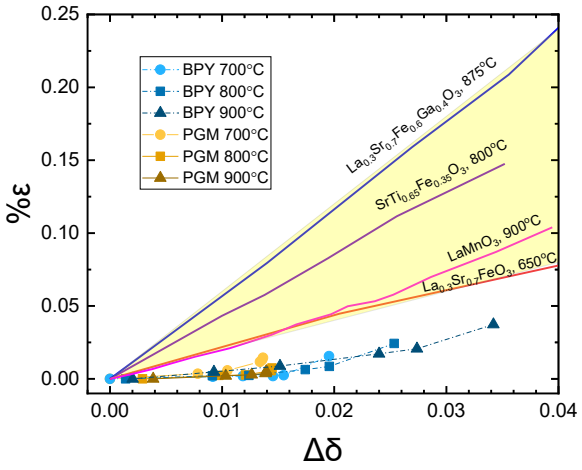

Figure 6. Comparison of data from this work with selected previously measured perovskites. The shaded region indicates the full range of redox CCEs previously measured and reported for perovskite materials[20,62,63]. The lowest strain values are set to zero for each sample and condition to better compare slopes.

Table 1. Summary of measured CCEs

PGM	**α_c**	**BPY**	**α_c**
700° C, low	0.005	700° C, low	0.0015
700° C, high	0.095	700° C, high	0.029
700° C, average	0.0086	**700° C, average**	0.011
800° C, low	0.003	800° C, low	0.0023
800° C, high	0.18	800° C, high	0.024
800° C, average	0.0056	**800° C, average**	0.009
900° C, low	0.003	900° C, low	0.007
900° C, high	0.18	900° C, high	0.020
900° C, average	0.0044	**900° C, average**	0.0058

Redox CCEs for previously studied perovskite compositions fall in the range of 0.02-0.06, while average CCEs in this work are 0.004-0.009 for PGM and 0.006-0.011 for BPY. For the temperature and pO_2 conditions reported here, PGM and BPY have redox CCEs that are as

much as 5 and 3 times lower, respectively, than those of any reported mixed conducting perovskite oxide redox CCEs, regardless of conditions.

Due to the anomalously low values of strain recorded for both BPY and PGM by dilatometry, the strains were further quantified using high temperature, in situ XRD in Ar and O_2. The two methods probe different length scales and thus provide slightly different information; dilatometry is a macroscopic measurement, while XRD monitors changes in all the unit cell lattice parameters. Rietveld refinements using TOPAS resulted in high quality fits with R_{wp} values less than 7.5% for all sample conditions. Figure 7 shows the quality of fits for selected data, and Figure 8a-b shows the lattice parameters from refinement. The results from structure refinement and the corresponding R_{wp} values are also listed in Table 2. For PGM at

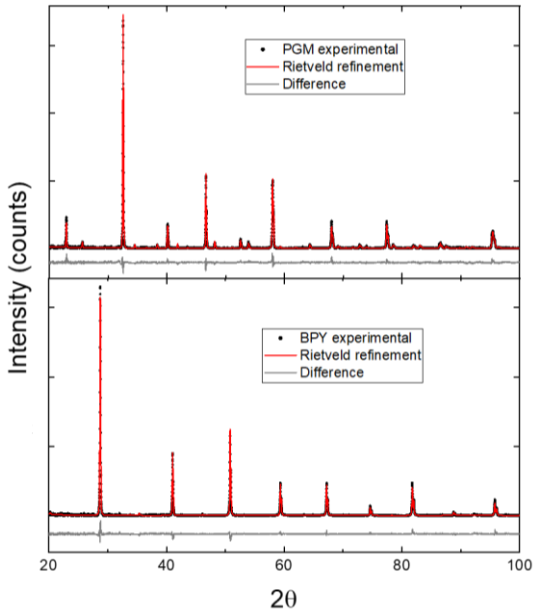

Figure 7. Visualization of the quality of Rietveld refinement for HTXRD scans at 700° C in O_2 for PGM (top) and BPY (bottom). The refinement model is the red line overlapping the experimental data (black dots), and the difference between these two is the grey line below each scan.

700° C, a and c lattice parameters increase upon oxygen loss while b decreases. At 900° C, a and b lattice parameters increase slightly with oxygen loss while c remains constant. BPY

shows an increase in lattice parameter upon oxygen loss for both the rhombohedral and cubic phases.

Scans were taken every 30 minutes during the isothermal holds to determine the degree of equilibration for each sample condition; Figure 9 shows the shift in a high angle peak for BPY at 900° C in Ar after the initial heating step from room temperature in Ar. The shift toward lower 2θ corresponds to the increase in lattice parameter upon reduction, and the peak positions converge within the last 60 minutes indicating that equilibrium had been reached. Time-dependent data indicated that the samples reached equilibrium in all conditions except the scan

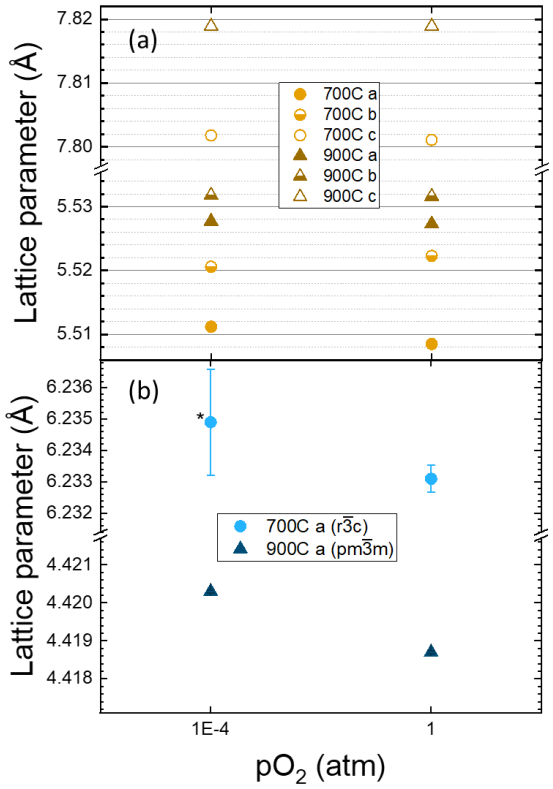

Figure 8. Lattice parameters for the Rietveld refinement of a) PGM: the phase is Pbnm for each temperature and pO_2 value, and b) BPY: the phase is $R\bar{3}c$ at 700° C and $Pm\bar{3}m$ at 900° C. Strain error bars for HTXRD are calculated from the lattice parameter refinement error. Error bars smaller than the symbols are not shown.
*this data point has large refinement errors due to a lack of equilibration at this measurement step.

Table 2. Refinement lattice parameters and fit value, R_{wp}. Numbers in parentheses indicate the applicable digit of uncertainty from refinement.

Sample	Condition (T, gas)	Phase	a (Å)	b (Å)	c (Å)	Cell Angle	R_{wp}
PGM	900° C, Ar	Pbnm	5.527(7)	5.531(8)	7.818(9)	90	7.45
	900° C, O_2	Pbnm	5.527(3)	5.531(6)	7.818(9)	90	6.13
	700° C, Ar	Pbnm	5.511(2)	5.520(6)	7.801(8)	90	7.21
	700° C, O_2	Pbnm	5.508(5)	5.522(3)	7.801(1)	90	5.68
BPY	900° C, Ar	$Pm\bar{3}m$	4.420(3)	-	-	90	6.66
	900° C, O_2	$Pm\bar{3}m$	4.418(7)	-	-	90	5.42
	700° C, Ar	$R\bar{3}c$	6.23(49)	-	-	59.9(97)	6.70
	700° C, O_2	$R\bar{3}c$	6.23(31)	-	-	60.0(01)	5.83

taken at 700° C in Ar for BPY. As described in the Methods section, the previous step was the isothermal hold at 900° C in Ar; because larger concentrations of oxygen vacancies tend to form at higher temperatures, the sample was in the process of oxidizing during the hold at 700° C.

The excess metastable oxygen vacancies during the measurement at 700° C in Ar, relative to the equilibrium state, resulted in artificially larger lattice parameters for this step, and this resulted in excess calculated strain for BPY at 700° C. Figure 2 shows the comparison between the linear strains calculated from HTXRD and from dilatometry. Despite the overestimation of strain for BPY at 700° C due to a lack of equilibration, there is very good agreement between

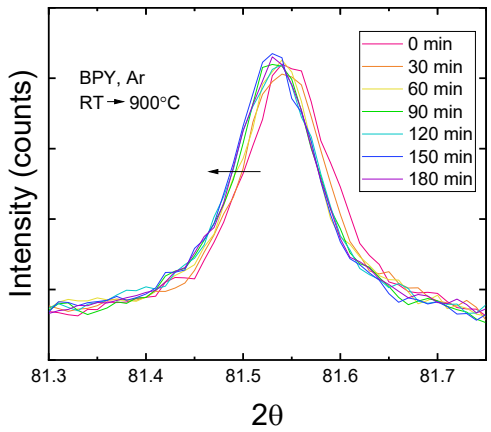

Figure 9. Time lapse of a selected, high angle peak of BPY after reaching 900° C from room temperature in Ar. The peak positions shift to lower angles, indicating larger d-spacing, as oxygen vacancies are introduced under high temperature and relatively low pO_2 conditions. Overlap of the 3 lowest angle peaks indicates convergence of the d-spacing by 120 min.

the dilatometry and HTXRD data; these results confirm the extremely low strains observed by dilatometry and indicate that the CCEs for BPY and PGM are the lowest ever recorded for perovskite materials, to our knowledge.

2.2. Computational CCE: Next, we present the computational results and a proposed contribution to the low CCEs of PGM and BPY on the basis of electronic structure. As explained in the Computational Methods section, an appropriate Hubbard *U* value is required to more accurately describe the Pr-*4f* states in DFT. The optimal value is not known, so we tested across a range of *U* values. The PDOS for each U considered is given in the SI for both materials (see Figure S9). For each material, we illustrate the effect of the parameter U on the electronic structure of the material which spans a range of behaviors, which in turn gives insights into how the chemical expansion is affected. Although a range of possible behaviors is obtained, we infer the appropriate atomistic chemical expansion mechanism from the experimentally found ultra-low CCEs. A more detailed study of the effect of the parameter *U* on these Pr oxide materials will be presented in a forthcoming publication[64].

Figure 10(a) shows a simplified depiction of the projected density of states (PDOS) of PGM when Mg dopant atoms are introduced to the system without any O vacancies (see Figure S10 for the actual calculated PDOS) For selected values of U = 4 eV and U = 10 eV. The principal difference arising from the choice of U lies in the relative positions of the filled Pr-*4f* states and the O-*2p* bands (see Figure S9 in SI). As the U value is increased the Pr-*4f* states become more localized and the separation between the lower and upper Pr-*4f* states widens. As the separation widens, the lower set of Pr-*4f* states eventually drop below the O-*2p* band. For *U* = 4 eV, the valence band maximum (VBM) consists of Pr-*4f* states, and Mg^{2+} is electronically

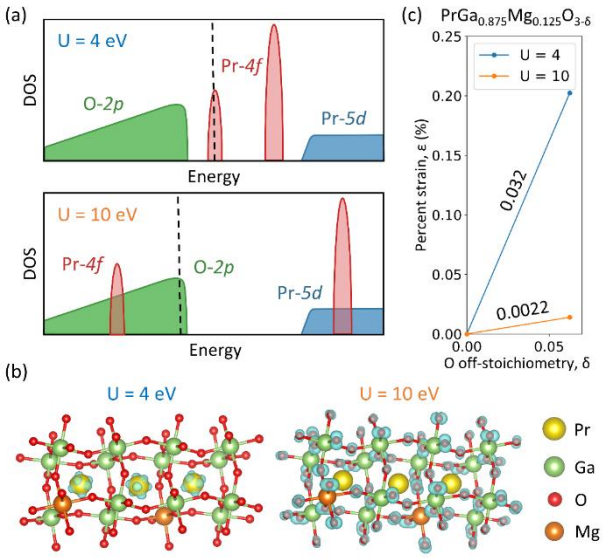

Figure 10. (a) Simplified depiction of the PDOS of PGM when Mg dopants are introduced without any O vacancies, the black dashed line represents the Fermi level. Pr-*4f* holes are formed at U = 4 eV, and O-*2p* holes are formed at U = 10 eV. (b) Partial charge density of the holes formed due to Mg doping, the charge density isosurface is shown in blue. (c) Plot of percent strain against δ for the two values of U = 4 and 10 eV, with their respective CCEs shown. All results are shown for the arrangement where the Mg atoms and O vacancy are far apart.

compensated by the formation of holes in the Pr-*4f* states. For U = 10 eV, the filled Pr-*4f* states drop below the O-*2p* band edge and, as a result, Mg^{2+} is now electronically compensated by O-*2p* holes instead of Pr-*4f* holes. The O-*2p* hole states are significantly more delocalized compared to the Pr-*4f* hole states, as shown by the partial charge density plots in Figure 10(b). Subsequently, when an O vacancy is introduced to the system, these hole states become filled by the two electrons left behind by the removed oxide ion (see Figure S10). Marrocchelli et al.[17] found that the filling of more delocalized Ce-*4f* states leads to a smaller increase in the ionic radius of Ce, resulting in a smaller chemical expansion in ceria. Likewise, a smaller chemical expansion is observed here when O-*2p* holes rather than Pr-*4f* holes are filled, as shown by the plot of strain versus O off-stoichiometry in Figure 10(c). Estimates of the CCEs are given by the slopes of the plots, and it is important to note that these are rough estimates due to the lack of additional data points and the large δ value (0.0625) compared to experiments, arising from supercell size limitations. Nonetheless, when O-*2p* holes are filled (U = 10 eV) the CCE is an order of magnitude smaller than when Pr-*4f* holes are filled (U = 4 eV). While the

exact positions of the Pr-*4f* and O-*2p* states are not known from experiment, we were able to find PES data for the related compound $PrInO_3$[68], which shares the same *Pbnm* space group as $PrGaO_3$, and the data indicates that the Pr-*4f* states are located slightly above the O states (see Figure S11a). This suggests that a U value roughly in the range of 6-8 eV may reasonably describe PGM in our simulations. Considering the unusually small CCEs found for PGM in the low Δδ region (refer to Table 1), we propose that doping $PrGaO_3$ with Mg forms a combination of Pr-*4f* and O-*2p* holes, or entirely O-*2p* holes. Subsequently, the filling of these less localized holes when O vacancies are formed leads to very small CCEs. On the other hand, the apparent large experimental CCEs in the high Δδ region (refer to Table 1) are an order of magnitude larger than the CCE for $U = 4$ eV when Pr-*4f* holes are filled, suggesting that they are caused by some other factor. The large CCE values for the high Δδ region listed in Table 1 may be artificially high due to the very small changes in Δδ and thus higher uncertainty.

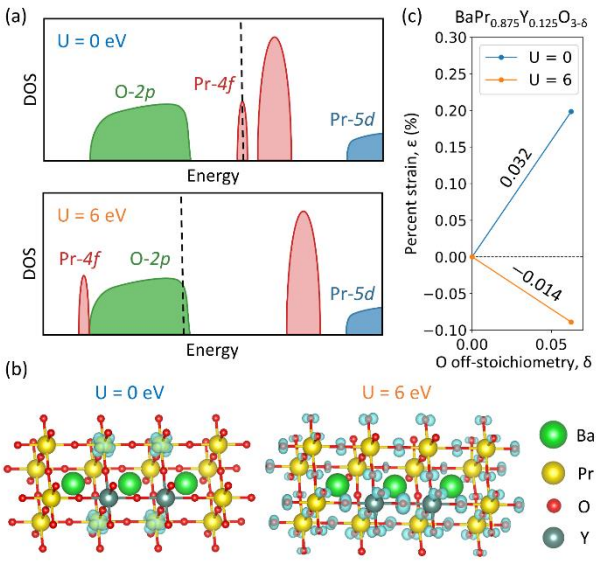

Figure 11. (a) Simplified depiction of the PDOS of BPY when Y dopants are introduced without any O vacancies, the black dashed line represents the Fermi level. Pr-*4f* holes are formed at U = 0 eV, and O-*2p* holes are formed at U = 6 eV. (b) Partial charge density of the holes formed due to Y doping, the charge density isosurface is shown in blue. (c) Plot of percent strain against δ for the two values of U = 0 and 6 eV, with their respective CCEs shown. All results are shown for the arrangement where the Y atoms and O vacancy are close together.

For BPY, the simplified PDOS when Y dopant atoms are introduced without any O vacancies is shown in Figure 11(a) (see Figure S12 for the actual calculated PDOS). Again, the electronic structure of BPY shows a similar behavior to PGM. Y^{3+} is electronically compensated by Pr-*4f* holes for $U = 0$ eV, and by O-*2p* holes for $U = 6$ eV due to the occupied Pr-*4f* states shifting lower in energy. Measurements from resonant PES (RPES) measurements of $BaPrO_{3-\delta}$ thin films performed by Higuchi et al. (see Figure S11) find the Pr states to be in close proximity to the O states, possibly slightly above or below depending on the synthesis conditions[65,66], and corresponding roughly to U = 2-4 eV in our simulations. As shown by the partial charge density plots in Figure 11(b), the Pr-*4f* hole states are localized to Pr atoms neighboring the Y atoms, whereas the O-*2p* hole states are delocalized throughout the cell. The plot of simulated strain against O sub-stoichiometry is given by Figure 11(c), and again a larger chemical expansion occurs when Pr-*4f* holes are filled ($U = 0$ eV). When O-*2p* holes are filled ($U = 6$ eV), the expansion of the lattice is not only smaller, but it in fact becomes negative (i.e., the lattice slightly contracts). This contraction arises from the arrangement of the Y dopant atoms and the O vacancy close together, and a similar behavior was found for PGM when the Mg atoms and the O vacancy were arranged close together. It is believed that chemical expansion arises mainly from the competition between (1) lattice expansion due to increases in ionic radius of reduced ions and (2) lattice contraction around the O vacancies due to electrostatic interactions[13,15,67]. If the latter effect is larger in magnitude, the introduction of a vacancy can result in a net contraction as observed here. Assuming that the lattice expansion due to reduction of ions is similar across different arrangements of dopant atoms and O vacancies, then the lattice contraction around O vacancies is larger when the dopants and vacancies are clustered together compared to when they are far apart. Note that the actual arrangement of Y atoms and O vacancies would most likely be different such that a small expansion is achieved as measured in the experiments. Nonetheless, as with PGM, we see that the filling of Pr-*4f* holes alone would give a much larger CCE than the experimental CCEs in

the low Δδ region (refer to Table 1), so the filling of O-*2p* holes to some extent is possible as well for BPY. In the high Δδ region, the increase in the experimental CCEs may be due to increased filling of Pr-*4f* holes, or some other undetermined factor.

Additionally, BPY demonstrates significant hybridization between Pr-*4f* and O-*2p* states, indicated by the considerable overlapping of these two states in the PDOS (see Figure S12). The presence of hybridized Pr-*4f*/O-*2p* states in $BaPrO_3$ has also been reported in literature[66,69], indicating appreciable covalent character in its Pr-O bond. This hybridization of Pr-*4f*/O-*2p* states would likely contribute to the charge delocalization in BPY, making it one of the possible reasons for the low CCEs observed. In contrast, PGM shows less overlapping of Pr-*4f* and O-*2p* states (see Figure S10). pCOHP analysis also show significantly larger magnitudes of pCOHP for Pr-O interactions in $BaPrO_3$ compared to $PrGaO_3$ (see Figure S13), confirming the higher Pr-O hybridization in the former. The higher covalency of the Pr-O bond in BPY compared to PGM is potentially due to the placement of Pr on the B-site instead of the A-site, since B-O bonds tend to be shorter than A-O bonds in perovskites, which may assist Pr-*4f* and O-*2p* orbital overlap. In PGM, on the other hand, even though Ga is located on the B-site, the degree of Ga-O hybridization is low near the top of the O states in the valence band, as evidenced by low magnitudes of pCOHP for Ga-O interactions in $PrGaO_3$, compared to, e.g., $LaGaO_3$ (see Figure S13).

2.3. Conductivity: As suggested by the computational results and previous studies, the degree of charge localization can play a large role in chemical expansion[17,19]. To investigate this quantity experimentally, temperature-dependent electrical conductivity experiments, via impedance spectroscopy, were carried out for both compositions in 21% O_2. Conductivity values are also important for the practical application of these mixed conductors. Nyquist plots of the impedance data for selected temperatures are shown in Figure 12a (PGM) and 12b (BPY). At each temperature point, $R_1(R_2Q)$ equivalent circuits were fit to the impedance data, given

the offset of the visible arc, and resistances were converted to conductivities using sample geometries. Arrhenius plots in Figure 13 show the temperature dependence of conductivity associated with R_1 (the high frequency offset resistance), and the slopes are related to the activation energies for PGM (a) and BPY (b), evaluated according to eq. 4 where the exponent, n, is -1; this choice of exponent is commonly used for adiabatic small polarons[70–72]. While the

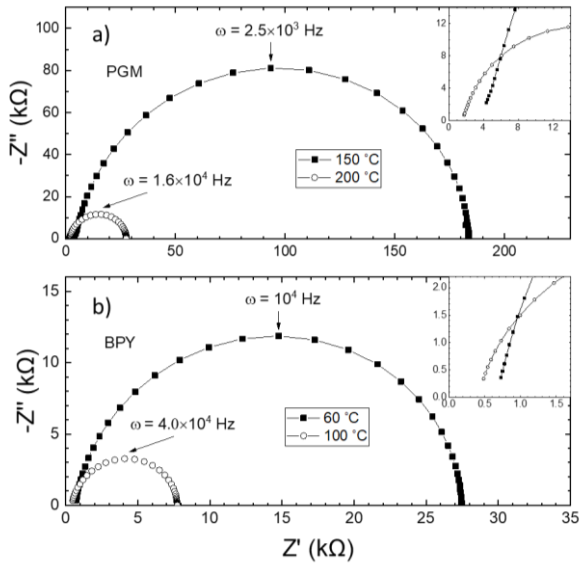

Figure 12. Nyquist plot for the impedance data of a) PGM at 150° and 200° C and b) BPY at 60° and 100° C. The relaxation frequency is shown for each data set, and the inset of each plot highlights the R_1 offset of each data set.

precise choice of exponent, and the corresponding model, is not fully known for these materials, the impact of the preexponential term on the calculated activation energies is very small and does not impact our analysis.

$$\sigma = \sigma_o T^n \exp\left(\frac{-E_a}{k_B T}\right) \quad (4)$$

Based on the activation energies calculated for R_1 and R_2, the frequency range in which they appear, and the high capacitance of the intermediate frequency arc, R_1 (at high frequency) is expected to be the grain resistance, and R_2 is expected to be grain boundary resistance. For the high frequency impedance feature, the activation energies are found to be 0.37 eV for PGM and

0.16 eV for BPY. These values are lower than what is observed for oxygen ion diffusion in perovskites[73] and are thus attributed to electronic carriers. Additionally, the magnitudes of the conductivity are consistent with electronic conduction, and predominant p-type conductivity for dry BPY was indicated previously[31]. Prior work on PGM with a lower acceptor (Mg) concentration suggested it was a mixed oxide ion and hole conductor in high temperature, non-

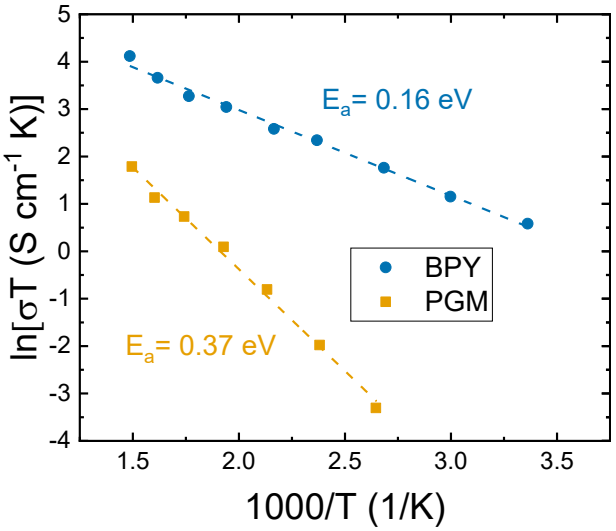

Figure 13. Arrhenius plots for grain conductivity of BPY and PGM. Conductivity calculated from R_1 in the equivalent circuit $R_1(R_2Q)$. Activation energies, E_a, are calculated from the linear fits shown by dashed lines.

reducing conditions[30], but the higher Mg concentration in the present work seems responsible for significant electronic compensation in these more oxidizing, low-temperature measurement conditions.

In general, activation energies may include a contribution from a migration energy and a contribution from a charge carrier (defect) formation energy. For electronic charge-carriers, the migration energy is influenced by charge trapping (e.g., polaron self-trapping energy)[74], and so this term is a direct indicator of charge localization and our term of interest. The second contribution, the charge-carrier formation energy, reflects changes in carrier concentration with temperature, which can be caused by a) redox reactions, b) generation of intrinsic electron-hole

pairs, or c) ionization processes, in which the carrier is promoted from a band to a mid-gap energy level (or vice versa). In order to try to isolate the migration energy term, contributions from carrier generation by redox reactions, intrinsic across-gap carrier generation, and mid-gap ionization were ruled out or deemed unlikely, as described next.

First, the effect of temperature-dependent redox reactions was evaluated by analyzing mass changes in the TGA across the temperature range of the impedance scans. Charge carrier concentration changes were calculated from the changes in mass, and corresponding percent changes in conductivity were determined using Equation 4. The calculated changes in conductivity from redox reactions were applied to the respective Arrhenius plots, and this adjustment resulted in less than 4% change in the calculated activation energies for both samples; this change is within error of experimental measurements and is considered negligible. Second, intrinsic carrier generation was ruled out, because the observed activation energies were significantly lower than half the expected band gaps: for undoped BPO, the gap has been reported to be about 2 eV[75] and undoped PGO is predicted to have a band gap >3 eV by first principles DFT calculations[76], in agreement with calculations made in this work. Further, considering the simulations in the present work, since O-*2p* holes are expected to form in both materials, PGM and BPY would be more appropriately described by using high U values. As such, intrinsic carrier generation would have to occur over wide band gaps (refer to Figure 10(a) for U = 10 eV and Figure 11(a) for U = 6 eV), so it is considered to be unlikely. Lastly, the possibility of mid-gap ionization is considered unlikely for these measurements, on the basis of the DFT-calculated densities of states, in which the required mid-gap states are not observed; however, it cannot be eliminated by these calculations alone. Nonetheless, after ruling out any significant contributions from changes in redox- or intrinsic-derived charge carrier concentration, the relatively low activation energies of 0.37 eV for PGM and 0.16 eV for BPY are most likely indicative of lower charge migration barriers in the BPY composition. These

activation energies would be consistent with small and large polaron self-trapping energies in PGM and BPY, respectively.

The conductivity measurement results match the expectation from our DFT simulations of a significant presence of O-*2p* hole states that are less localized than Pr-*4f* states in PGM and BPY. Although the proportion of O-*2p* holes compared to Pr-*4f* holes is not precisely known *a priori*, the lower activation energy for BPY compared to PGM suggests that the holes are more delocalized in BPY than in PGM. Hybridized Pr-*4f*/O-*2p* states should also be present in BPY as mentioned previously, contributing to the charge delocalization in BPY. In other words, we speculate that the apparent large polaron behavior of BPY may be attributed to greater hybridization of Pr-*4f*/O-*2p* states at the Fermi level, while the apparent small polaron behavior of PGM may indicate more charge localization on *O-2p* states at the top of its valence band with deeper Pr-*4f* levels (or vice versa).

3. DISCUSSION

The average macroscopic coefficients of chemical expansion for reduction of both BPY and PGM are lower than any previously reported perovskite oxide CCE. The low value of strain is confirmed by *in situ* HTXRD, and the chemical expansion mechanism is probed by DFT. In what follows, we provide some possible explanations for the low CCEs, identify the most likely contributing factor(s), and propose some guidelines for future design of low-CCE perovskites that undergo redox.

3.1. Indeterminate Contributor to Low CCE: A- vs. B-Site Placement of Multivalent Cation: Returning to one motivation for this study, we consider the impact on CCE of the placement of the potentially multivalent cation, Pr. As noted in the introduction, application of an empirical model of perovskite lattice parameters by Marrocchelli et al.[15] suggests that equal increases in cation radius result in a larger increase in lattice parameter when the cation expands at the B-

site rather than at the A-site. This model was summarized by Equation 3 in the introduction. Using a relatively small effective oxygen vacancy radius of 1.3 Å and Shannon ionic radii, estimates for CCEs of BPY and PGM were made by determining lattice parameters with varying concentrations of oxygen vacancies and the corresponding Pr^{4+}/Pr^{3+} concentrations. This estimation results in a CCE of ~0.08 for BPY and ~0.04 for PGM if the oxygen loss is accommodated by the reduction of Pr ions only. The experimentally measured CCEs are much smaller than these predictions. We suggest one major reason for the discrepancy is that it is more likely that the reduction of O ions is taking place instead of, or in addition to, Pr ions. Unfortunately, CCE predictions for O ion reduction cannot be made with the empirical model, since the Shannon ionic radius for O^- is not available.

To examine the impact of cation site placement in another way, we can compare the predictions of the empirical model to our DFT results for the case where the filling of Pr-*4f* holes occurs (PGM for $U = 4$ eV and BPY for $U = 0$ eV). In the arrangement where the dopants (Mg or Y) and vacancy are close together, the computational CCEs for BPY and PGM are approximately 0.032 and 0.018 respectively. Although the CCE is dependent on the dopant and vacancy arrangement, the ratio of BPY to PGM CCE values calculated by DFT (with hole localization on Pr) is consistent with that of the empirical model; this result suggests that the discrepancy in CCE magnitude may be largely due to dopant and vacancy relative arrangement. Regardless, the DFT-simulated CCE is lower when the multivalent cation is located on the A-site rather than the B-site, as predicted by the empirical model. This result suggests that the effect of A- vs. B-site cation placement may become important for highly ionic perovskites where charge does localize on the multivalent cation, in which case A-site placement is preferable, when possible. The quantitative discrepancy between the (low U) DFT and empirical models may also be accounted for by assumptions in the empirical model that are not valid for BPY and PGM, the most critical assumptions being a cubic structure, full charge

localization, and no subtle symmetry changes upon reduction. Particularly, BPY demonstrates prominent covalent character in its bonding, resulting in hybridized states, whereas the empirical model assumes predominantly ionic character in the bonding. The covalent character of BPY is also supported by the measured high conductivity and low activation energy. As we noted above, it seems plausible from the BPY vs. PGM activation energy comparison and A-O vs. B-O bond length considerations that B- vs. A-site Pr site placement may play a role in favoring covalency through Pr-*4f* / O-*2p* orbital overlap, thus countering the prediction of the fully ionic empirical model. Breaking from the abovementioned assumptions as well as the involvement of charge located on oxygen are the most likely reasons for the low observed CCEs regardless of Pr site occupancy, as discussed below.

3.2. Possible Contributor to Low CCE: Low Unit Cell Symmetry: Unit cell symmetry has been suggested to play a role in the degree of chemical expansion exhibited by mixed conducting perovskites, where lower symmetry phases can expand anisotropically, and macroscopically less than their symmetric counterparts, during oxygen loss[1,19,77]. Here, we consider the effect of crystallographic symmetry on CCEs of PGM and BPY in the present study. Orthorhombic PGM (700-900^{o} C) may be considered the lowest symmetry phase of those studied, as there are three different unit cell axis lengths, and the octahedral rotation pattern, $a^{-}a^{-}c^{+}$, has a unique magnitude and rotation sense along the z-axis vs. the other axes. Rhombohedral BPY (700^{o} C) is the next lowest symmetry phase with uniform unit cell lengths and rotation pattern $a^{-}a^{-}a^{-}$, and cubic BPY (900^{o} C) is the undistorted perovskite with uniform unit cell lengths and no octahedral rotations – therefore highest symmetry. Comparing average CCEs, cubic BPY has a larger value at 0.011 than rhombohedral BPY at 0.0058, consistent with the expectation from symmetry. For comparison, chemical expansion in rhombohedral, Sr-doped $LaFeO_3$ has been discussed elsewhere[78] and the authors show that more reducing atmospheres induce a decrease in both the rhombohedral angle (between axes) and the octahedral rotation angle. A decrease in

the rhombohedral angle, α, decreases the volume of the cell for a given lattice parameter, so the decrease in α upon reduction may decrease the net chemical expansion in rhombohedral phases. Rhombohedral phases may also be more likely to accommodate defect-induced strain through distortions of their octahedra, rather than the uniform or isotropic cell expansion observed in cubic phases.

Although compounding factors make it difficult to draw conclusions from a comparison of phase and CCE between PGM and BPY, we can analyze the expansion in orthorhombic PGM to gain insights into how its axis-resolved strain may contribute to the very low observed CCEs. Differences in unit cell lengths and octahedral rotation angles along the three crystallographic axes correspond to variations in chemical expansion values along these axes, which can be determined from the HTXRD refinements. At 700^{o} C with pO_2 changing from 1 to 10^{-4} atm, the a-axis had the smallest lattice parameter, yet it expanded the most upon reduction with a 0.05% strain. The b-axis contracted with a -0.03% strain, and the c-axis had very little expansion with 0.009% strain. The anisotropic expansion is validated by DFT in Figure S15, and it can be seen qualitatively in Figure 14 by the change in peak shape and shifting of the hkl indices. As the material reduces, hkl indices weighted more on the b-axis (132, 024) can be seen to move to lower d-spacing (higher angle), and hkl indices with little or no b-axis contribution can be seen to move to larger d-spacing (204, 312). As lattice parameters diverge, there is less overlap of the hkl indices, and distinct peaks become more visible for the oxidized case. For comparison, orthorhombic $Sr(Sn,Fe)O_{3-x}$ was shown to exhibit only slightly anisotropic reduction-induced strains and significantly lower CCE than its isotropically straining, cubic counterpart $Sr(Ti,Fe)O_{3-x}$[77]. In the present work, the orthorhombic PGM phase demonstrates considerably more anisotropic chemical strain, with contraction and expansion both present. This effect could contribute to lowering macroscopic CCEs. However, we note that among the literature reports of various mixed conducting perovskites, no CCEs as low as

those in the present work have so far been demonstrated for low symmetry systems. Therefore we expect that other factors beyond symmetry also are needed to accomplish the very low CCEs.

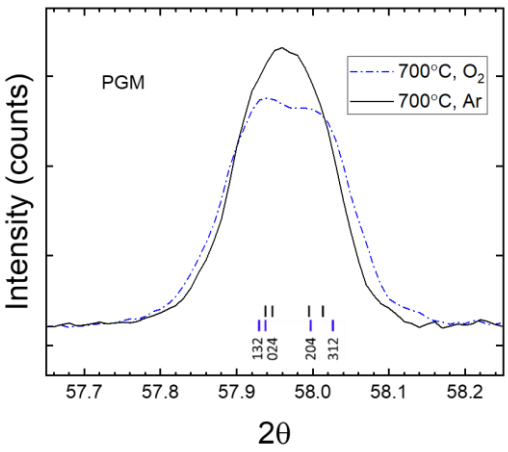

Figure 14. Selection of hkl indices exhibiting anisotropic expansion upon reduction at 700° C. Black hkl ticks (top) correspond to the reducing condition, Ar, and blue ticks (bottom) correspond to the oxidizing condition, O_2.

3.3. Possible Contributor to Low CCE: Charge Delocalization: In previous works[17,19,20], a higher degree of charge localization was associated with a higher CCE. As noted in the results section, we assessed the degree of charge localization from the conductivity activation energies, by ruling out all contributions to the thermal activation except mobility (and separating out the apparent grain boundary contribution). Higher activation energies thus corresponded to larger barriers for charge migration or greater charge trapping, i.e., greater localization. The experimental activation energies for grain conductivity from the results in Figure 13 suggest that PGM may have a higher degree of charge localization than BPY. However, PGM also has lower CCEs than BPY for most conditions, which is not explained by this result. Further, neither composition exhibits full charge delocalization, i.e., metallic behavior, but rather some degree of localization as small (PGM) vs. large (BPY) polarons is still suggested electrically. Thus the partial charge delocalization in this work does not appear to explain fully the anomalously low CCEs. On the other hand, the temperature dependence of mobility could still contribute to the

temperature dependence of CCEs in the present work to some extent. For example, the larger increase in charge mobility with temperature for PGM (higher activation energy) may contribute to the lower CCEs at higher temperatures. Although the charge mobility also increases with temperature in BPY, this smaller increase in charge mobility appears to be overshadowed by the changes in unit cell symmetry described above.

It should be noted that prior work highlighting the potential impact of localization focused on cation charge localization specifically. For example, in simulations of CeO_{2-x} reduction, artificial delocalization of Ce-*4f* electrons gave rise to ~70% lower CCEs[17]. Similarly in experimental measurements of $La_{0.9}Sr_{0.1}Ga_{1-x}Ni_xO_{3-\delta}$[19] and $SrTi_{1-x}Fe_xO_{3-\delta}$[20], the charge localization was decreased by raising the potentially multivalent cation concentration x, with the idea that the Ni-*3d* and Fe-*3d* states, respectively, would broaden around the Fermi level and increase mobility; such changes gave rise to 10-40% CCE decreases. None of the prior work indicating a role of localization has explicitly considered the role of anion charge localization. Thus in our next point, we consider charge location on anions vs. cations, which may be a key factor in the present study.

3.4. Likely Contributor to Low CCE: Charge Location on Oxygen: For both PGM and BPY, the DFT+U results suggest that the location of the hole (or redox process or multivalency) on anions vs. cations has a significant impact on CCE. Depending on the value of the Hubbard U, the lower energy Pr-*4f* states may lie at the top of the valence band (Pr-*4f* holes), overlap with O-*2p* states near the Fermi level (holes shared by O and Pr), or lie below the O-*2p* states and Fermi level (O-*2p* holes). The simulations showed that when O-*2p* holes rather than Pr-*4f* holes become the primary electronic defect compensating for the acceptors, the values for redox-induced chemical expansion decrease significantly. As noted in the computational results section, the O-*2p* states are more delocalized than the Pr-*4f* states, which may partially explain the trend. The oxygen evolution (redox) reaction involving O-site polarons (filling of holes

located on oxygen) is shown in Equation 5, and reduction involving the multivalent cation (filling of holes located on Pr) is shown in Equation 6.

$$2O_O^{\bullet} \rightleftharpoons v_O^{\bullet\bullet} + O_O^{\times} + \frac{1}{2}O_2 \quad (5)$$

$$O_O^{\times} + 2Pr_{Pr}^{\bullet} \rightleftharpoons v_O^{\bullet\bullet} + 2Pr_{Pr}^{\times} + \frac{1}{2}O_2 \quad (6)$$

The role of anion vs. cation charge location on CCEs has not been widely explored, but we note one supportive result in our prior work with S. Ricote, where $BaZr_{0.9}Y_{0.1}O_{3-\delta}$ with holes on oxygen (oxygen polarons) exhibited negligible redox strain compared to $BaZr_{0.9}Dy_{0.1}O_{3-\delta}$, with charge at least somewhat on Dy with significant redox strain[37]. Further, we note the very low CCEs of Pr-bearing perovskites in the present work contrast with the high measured CCE (0.087) of mixed-conducting fluorite $Pr_{0.1}Ce_{0.9}O_{2-\delta}$ where charge is thought to localize on Pr under oxidizing conditions[79].

3.5. Toward Generalized Design Rules for Low CCE: The discussion above relating to trends in CCE with composition and temperature leads to potentially generalized design rules that can be used to tailor chemical expansion. Factors that influence chemical expansion, such as the degree of charge localization, unit cell symmetry, symmetry changes upon reduction, and multivalent cation placement, have been discussed here and elsewhere[15,17,19,80,81]. The general expected and observed trends are that a higher degree of symmetry, higher degree of charge localization (on cations), and multivalent cations on the B-site in ionically bonded systems all lead to higher CCE. In the present work we further highlight the role of charge *location* (i.e., the nature of orbitals involved in redox). While it is true that localizing charge on multivalent cations results in an increase in chemical expansion, filling of holes that are preferentially located on oxygen can yield a smaller CCE. The location of charge may also be a reason for the nonlinearity seen in both materials. As a material oxidizes, the hole concentration increases, and the Fermi level decreases down to deeper states in the valence band. This change may affect

the character of the holes. For example, if Pr levels lie below O levels, as the Fermi level drops the holes are no longer located only on the O-*2p* orbitals, and the CCE may increase as charge is shared with Pr. The possible existence of some "Pr^{4+}" (hole located on Pr) in PGM has been suggested by Liu *et al*[30]. Other potential reasons for the nonlinearity in the present work are increasing defect association with increasing hole concentration[82] and slight changes in crystal symmetry upon reduction.

3.6. Band structure design for low CCE materials: Designing perovskite materials that will fill O-*2p* holes upon reduction typically involves selecting compositions with O-*2p* derived states at the top of the valence band. Determining the composition that will give rise to a desired band structure ("inverse design") is often a difficult task requiring high-throughput computational simulations that may compromise on accuracy. As seen in the present work, from a DFT+U standpoint, one of the challenges in determining the character of the valence band maximum is setting an appropriate U value, since this term impacts the energy splitting of the metal states. However, some first-order strategies can be implemented to start. For example, one may pursue computationally inexpensive estimates of band structures, using combinations and interpolations of known compound data. Thimsen et al.[83] developed a Mixed Metal Oxide Band Structure (MMOBS) procedure to predict the electronic structures of mixed transition metal oxides using catalogued band position data of the basis oxides, weighted by fraction. Results of their procedure agreed with first-principles DFT calculations and experimental measurements for the mixed Ti-Fe-O compounds, and the authors claim that it has also been effective for Ti-V-O and Ti-Ni-O systems. Significant differences in crystal structure can cause challenges for this approach, however. An alternative strategy is to focus on stoichiometric tailoring of a given composition. One may shift the Fermi level in the valence band through modifying the ratios of cations of different valences and/or the oxygen stoichiometry. By this strategy, it may be possible to move the Fermi level into O-*2p*-dominated states; nonetheless, the band structure

would need to be known at the outset. Deml et al.[84] investigated the effect of cation mole fractions on the oxygen vacancy formation energies and position of the Fermi level relative to the O-*2p* band center in $Sr_xLa_{1-x}Mn_yAl_{1-y}O_3$. Adjusting the mole fraction of Sr (χ_{Sr}) and Mn (χ_{Mn}) changed the hole concentration and the character of the corresponding unoccupied states. For example, when $\chi_{Sr} > \chi_{Mn}$, the Fermi level moved into the O-*2p* states, because more holes were generated from Sr-substitution than the density of states in the mixed Mn-*3d* / O-*2p* band. Similarly, strain may be used to modulate point defect concentrations and electronic structure. For small modifications to the band structure, Hwang et al.[85] discussed how strain may be applied to upshift (tensile) or downshift (compressive) the *O-2p* states, and DFT calculations showed that compressive strain increases the width of the *d*-band for Sr and La-based A-site perovskites with a range of Period 4 transition metals[86].

While filling of O-*2p* holes may give rise to low CCEs, the DFT results from our work have also indicated that a reason for the low experimental CCE in BPY is the sharing of charge between Pr and O. Valence band metal-oxygen hybridization may therefore be a second potential design principle for perovskite selection for low CCE applications. For d-electron perovskites, Zimmerman et al.[87] demonstrated that the degree of covalency increases as the number of empty *d*-states increases. Suntivich et al.[88] suggest, however, that an e_g-filling descriptor is more accurate than a *3d*-filling descriptor (consisting of both t_{2g} and e_g electrons) because the σ-bonding e_g orbital has a stronger overlap with oxygen than the π-bonding t_{2g} orbital. Kaindl et al.[89] observed a similar trend for *f*-electron elements with their theoretical analysis. They found that covalency is stronger for light Ln element Pr than heavier element Tb. B site cation-oxygen covalency in perovskites is also influenced by the octahedral tilting angles, which affects orbital overlap[90], and may be tailored by the size of the A-site cation. We further hypothesize that B-site placement of the potentially multivalent cation may favor covalency with oxygen compared to A-site placement based on bond length considerations and

the results for electrical hole behavior in BPY (more delocalized) vs. PGM (more localized). Whether or not this last idea is correct, it is clear from the present work that Pr may be an excellent choice for compositions requiring low CCEs due to the high covalency on the B-site, O states near the Fermi level under oxidizing conditions, and the potential for either A- or B-site occupancy.

4. CONCLUSIONS

The near-zero average strains during redox observed in this work for $PrGa_{0.9}Mg_{0.1}O_3$ (PGM) and $BaPr_{0.9}Y_{0.1}O_3$ (BPY), provide insights into the rational design of materials that are vulnerable to chemo-mechanical failure or performance degradation due to spatial/temporal oxygen activity gradients. In general, perovskite-structured materials allow for a high degree of tunability in composition and symmetry variants that have direct effects on their observed properties; however, structure-property relationships can be difficult to predict due to the complexity and inter-dependencies of point defect chemistry, crystal structure, electronic structure, and properties affected by elemental substitution in perovskites. Stoichiometric chemical expansion is one such property, where as we have demonstrated, simple empirical models using ionic radii are insufficient to predict quantitatively the complex ionic and electronic point-defect-mediated lattice distortions that ultimately give rise to mechanical degradation. Instead, crystal-chemical design rules informed by quantum mechanical simulations and *in situ* characterization are needed to mitigate this strain in devices including fuel cells, electrolysis cells, gas separation membranes, electrochemical generators, and batteries. Here, we have shown how a combination of anisotropic expansion in distorted structures, charge delocalization, and particularly charge location on oxygen lead to anomalously low redox coefficients of chemical expansion for PGM and BPY, much lower than any previously reported value for perovskites, with significant promise for chemo-mechanical durability. While A- vs. B-site placement of the multivalent cation may be beneficial in

perovskites with charge location on that cation and highly ionic bonding, this effect is not dominant in partially covalent systems and/or systems with charge location on oxygen. We emphasize the benefit of O-*2p* orbitals at the top of the valence band (at the Fermi level in these p-type systems), with or without hybridization to the potentially multivalent cations, to minimize redox chemical strains. This observed relationship between band structure and chemical strain for the perovskite structure has potential as a broader design principle to lead to discovery of chemo-mechanically stable materials with earth-abundant elements to reduce environmental and societal impact while also reducing cost.

ACKNOWLEDGEMENTS

This work was supported financially by a NSF CAREER grant to NHP (DMR-1945482) and by initial funding from NSF grant no. 1545907 through a JSPS-NSF Partnership for International Research and Education (PIRE). The use of facilities and instrumentation was supported by NSF through the University of Illinois Materials Research Science and Engineering Center (DMR-1720633) and by the Materials Research Laboratory Central Research Facilities, University of Illinois for SEM work with the JEOL JSM-7000F Analytical SEM. Authors acknowledge use of TGA instrumentation at Kyushu University in the International Institute for Carbon Neutral Energy Research (WPI-I2CNER), sponsored by the Japanese Ministry of Education, Culture, Sports, Science and Technology. Computational work was performed on the Illinois Campus Cluster, a computing resource that is operated by the Illinois Campus Cluster Program (ICCP) in conjunction with the National Center for Supercomputing Applications (NCSA) and which is supported by funds from the University of Illinois Urbana-Champaign.

SUPPORTING INFORMATION DESCRIPTION

The supporting information document contains diffraction data, semiraw and uncorrected data, chemical strain without thermal contributions, DFT desity of states, DFT chemical strain of PGM along different unit cell axis, and data for thermochemical expansion.

CONFLICTS OF INTEREST

There are no conflicts to declare.

REFERENCES

(1) Frade, J. R. Challenges Imposed by Thermochemical Expansion of Solid State Electrochemical Materials. *Green Energy Technol.* **2013**. https://doi.org/10.1007/978-1-4471-4456-4_5.

(2) Adler, S. B. Chemical Expansivity of Electrochemical Ceramics. *J. Am. Ceram. Soc.* **2004**. https://doi.org/10.1111/j.1151-2916.2001.tb00968.x.

(3) Im, H. N.; Jeon, S. Y.; Choi, M. B.; Park, J. Y.; Song, S. J. Chemical Expansion of Water Splitting Oxygen Separation Membranes of La 0.7Sr 0.3Cu 0.2Fe 0.8O 3-δ. *J. Ceram. Process. Res.* **2012**, *13* (5), 579–585.

(4) Hutchings, K. N.; Bai, J.; Cutler, R. A.; Wilson, M. A.; Taylor, D. M. Electrochemical Oxygen Separation and Compression Using Planar, Cosintered Ceramics. *Solid State Ionics* **2008**. https://doi.org/10.1016/j.ssi.2008.02.058.

(5) Bishop, S. R.; Marrocchelli, D.; Chatzichristodoulou, C.; Perry, N. H.; Mogensen, M. B.; Tuller, H. L.; Wachsman, E. D. Chemical Expansion: Implications for Electrochemical Energy Storage and Conversion Devices. *Annu. Rev. Mater. Res.* **2014**. https://doi.org/10.1146/annurev-matsci-070813-113329.

(6) Zhang, W.; Schröder, D.; Arlt, T.; Manke, I.; Koerver, R.; Pinedo, R.; Weber, D. A.; Sann, J.; Zeier, W. G.; Janek, J. (Electro)Chemical Expansion during Cycling: Monitoring the Pressure Changes in Operating Solid-State Lithium Batteries. *J. Mater. Chem. A* **2017**. https://doi.org/10.1039/c7ta02730c.

(7) Malavé, V.; Berger, J. R.; Martin, P. A. Concentration-Dependent Chemical Expansion in Lithium-Ion Battery Cathode Particles. *J. Appl. Mech. Trans. ASME* **2014**. https://doi.org/10.1115/1.4027833.

(8) Strauss, F.; de Biasi, L.; Kim, A.-Y.; Hertle, J.; Schweidler, S.; Janek, J.; Hartmann, P.; Brezesinski, T. Rational Design of Quasi-Zero-Strain NCM Cathode Materials for Minimizing Volume Change Effects in All-Solid-State Batteries. *ACS Mater. Lett.* **2020**. https://doi.org/10.1021/acsmaterialslett.9b00441.

(9) Swallow, J. G.; Kim, J. J.; Maloney, J. M.; Chen, D.; Smith, J. F.; Bishop, S. R.; Tuller, H. L.; Van Vliet, K. J. Dynamic Chemical Expansion of Thin-Film Non-Stoichiometric Oxides at Extreme Temperatures. *Nat. Mater.* **2017**. https://doi.org/10.1038/nmat4898.

(10) Nicholas, J. D. Practical Considerations for Reliable Stress and Oxygen Surface Exchange Coefficients from Bilayer Curvature Relaxation Measurements. *Extrem. Mech. Lett.* **2016**. https://doi.org/10.1016/j.eml.2016.04.006.

(11) Balke, N.; Kalnaus, S.; Dudney, N. J.; Daniel, C.; Jesse, S.; Kalinin, S. V. Local Detection of Activation Energy for Ionic Transport in Lithium Cobalt Oxide. *Nano Lett.* **2012**. https://doi.org/10.1021/nl300219g.

(12) Chatterjee, A.; Caicedo, J. M.; Ballesteros, B.; Santiso, J. An in Operando Study of Chemical Expansion and Oxygen Surface Exchange Rates in Epitaxial GdBaCo2O5.5 Electrodes in a Solid-State Electrochemical Cell by Time-Resolved X-Ray Diffraction. *J. Mater. Chem. A* **2018**. https://doi.org/10.1039/c8ta02790k.

(13) Chatzichristodoulou, C.; Norby, P.; Hendriksen, P. V.; Mogensen, M. B. Size of Oxide Vacancies in Fluorite and Perovskite Structured Oxides. *J. Electroceramics* **2015**. https://doi.org/10.1007/s10832-014-9916-2.

(14) Marrocchelli, D.; Bishop, S. R.; Kilner, J. Chemical Expansion and Its Dependence on the Host Cation Radius. *J. Mater. Chem. A* **2013**. https://doi.org/10.1039/c3ta11020f.

(15) Marrocchelli, D.; Perry, N. H.; Bishop, S. R. Understanding Chemical Expansion in

Perovskite-Structured Oxides. *Phys. Chem. Chem. Phys.* **2015**. https://doi.org/10.1039/c4cp05885b.

(16) Jedvik, E.; Lindman, A.; Benediktsson, M. P.; Wahnström, G. Size and Shape of Oxygen Vacancies and Protons in Acceptor-Doped Barium Zirconate. *Solid State Ionics* **2015**, *275*, 2–8. https://doi.org/10.1016/j.ssi.2015.02.017.

(17) Marrocchelli, D.; Bishop, S. R.; Tuller, H. L.; Watson, G. W.; Yildiz, B. Charge Localization Increases Chemical Expansion in Cerium-Based Oxides. *Phys. Chem. Chem. Phys.* **2012**. https://doi.org/10.1039/c2cp40754j.

(18) Marrocchelli, D.; Chatzichristodoulou, C.; Bishop, S. R. Defining Chemical Expansion: The Choice of Units for the Stoichiometric Expansion Coefficient. *Phys. Chem. Chem. Phys.* **2014**. https://doi.org/10.1039/c4cp01096e.

(19) Perry, N. H.; Bishop, S. R.; Tuller, H. L. Tailoring Chemical Expansion by Controlling Charge Localization: In Situ X-Ray Diffraction and Dilatometric Study of (La,Sr)(Ga,Ni)O3-δ Perovskite. *J. Mater. Chem. A* **2014**. https://doi.org/10.1039/c4ta02972k.

(20) Perry, N. H.; Kim, J. J.; Bishop, S. R.; Tuller, H. L. Strongly Coupled Thermal and Chemical Expansion in the Perovskite Oxide System Sr(Ti,Fe)O3-α. *J. Mater. Chem. A* **2015**. https://doi.org/10.1039/c4ta05247a.

(21) Kharton, V. V.; Patrakeev, M. V.; Tsipis, E. V.; Avdeev, M.; Naumovich, E. N.; Anikina, P. V.; Waerenborgh, J. C. Oxygen Nonstoichiometry, Chemical Expansion, Mixed Conductivity, and Anodic Behavior of Mo-Substituted Sr3Fe2O7-δ. *Solid State Ionics* **2010**. https://doi.org/10.1016/j.ssi.2010.06.004.

(22) Kharton, V. V.; Kovalevsky, A. V.; Avdeev, M.; Tsipis, E. V.; Patrakeev, M. V.; Yaremchenko, A. A.; Naumovich, E. N.; Frade, J. R. Chemically Induced Expansion of La2NiO4+δ-Based Materials. *Chem. Mater.* **2007**. https://doi.org/10.1021/cm070096x.

(23) Tsvetkov, D. S.; Ivanov, I. L.; Malyshkin, D.; Sereda, V. V.; Zuev, A. Y. Mechano-

Chemical Coupling in Double Perovskites as Energy Related Materials. *ECS Trans.* **2016**. https://doi.org/10.1149/07224.0021ecst.

(24) Zuev, A. Y.; Sereda, V. V.; Tsvetkov, D. S. Defect Structure and Defect-Induced Expansion of MIEC Oxides: Doped Lanthanum Cobaltites. *J. Electrochem. Soc.* **2012**. https://doi.org/10.1149/2.061209jes.

(25) Kim, N.; Perry, N. H.; Ertekin, E. Atomic Modeling and Electronic Structure of Mixed Ionic-Electronic Conductor SrTi1- XFexO3- x/2+δ Considered as a Mixture of SrTiO3 and Sr2Fe2O5. *Chem. Mater.* **2019**, *31* (1), 233–243. https://doi.org/10.1021/acs.chemmater.8b04284.

(26) Harrington, G. F.; Sun, L.; Yildiz, B.; Sasaki, K.; Perry, N. H.; Tuller, H. L. The Interplay and Impact of Strain and Defect Association on the Conductivity of Rare-Earth Substituted Ceria. *Acta Mater.* **2019**. https://doi.org/10.1016/j.actamat.2018.12.058.

(27) Verma, A. S.; Jindal, V. K. Lattice Constant of Cubic Perovskites. *J. Alloys Compd.* **2009**. https://doi.org/10.1016/j.jallcom.2009.06.001.

(28) Jiang, L. Q.; Guo, J. K.; Liu, H. B.; Zhu, M.; Zhou, X.; Wu, P.; Li, C. H. Prediction of Lattice Constant in Cubic Perovskites. *J. Phys. Chem. Solids* **2006**. https://doi.org/10.1016/j.jpcs.2006.02.004.

(29) Ubic, R.; Subodh, G. The Prediction of Lattice Constants in Orthorhombic Perovskites. *J. Alloys Compd.* **2009**. https://doi.org/10.1016/j.jallcom.2009.08.139.

(30) Liu, Z.; Zheng, Z.; Huang, X.; Lü, Z.; He, T.; Dong, D.; Sui, Y.; Miao, J.; Su, W. The Pr4+ Ions in Mg Doped PrGaO3 Perovskites. *J. Alloys Compd.* **2004**. https://doi.org/10.1016/S0925-8388(03)00484-5.

(31) Knee, C. S.; Magrasó, A.; Norby, T.; Smith, R. I. Structural Transitions and Conductivity of BaPrO3 and BaPr 0.9Y0.1O3-δ. *J. Mater. Chem.* **2009**. https://doi.org/10.1039/b820976f.

(32) Magrasó, A.; Haugsrud, R.; Segarra, M.; Norby, T. Defects and Transport in Gd-Doped BaPrO3. *J. Electroceramics* **2009**. https://doi.org/10.1007/s10832-008-9541-z.

(33) Mimuro, S.; Shibako, S.; Oyama, Y.; Kobayashi, K.; Higuchi, T.; Shin, S.; Yamaguchi, S. Proton Incorporation and Defect Chemistry of Yb-Doped BaPrO3. *Solid State Ionics* **2007**. https://doi.org/10.1016/j.ssi.2007.02.006.

(34) Yadav, T. P.; Srivastava, O. N. Synthesis of Nanocrystalline Cerium Oxide by High Energy Ball Milling. *Ceram. Int.* **2012**. https://doi.org/10.1016/j.ceramint.2012.04.025.

(35) Indris, S.; Bork, D.; Heitjans, P. Nanocrystalline Oxide Ceramics Prepared by High-Energy Ball Milling. *J. Mater. Synth. Process.* **2000**. https://doi.org/10.1023/A:1011324429011.

(36) Vasylechko, L.; Pivak, Y.; Senyshyn, A.; Savytskii, D.; Berkowski, M.; Borrmann, H.; Knapp, M.; Paulmann, C. Crystal Structure and Thermal Expansion of PrGaO3 in the Temperature Range 12-1253 K. *J. Solid State Chem.* **2005**. https://doi.org/10.1016/j.jssc.2004.10.005.

(37) Ricote, S.; Hudish, G.; O'Brien, J. R.; Perry, N. H. Non Stoichiometry and Lattice Expansion of BaZr0.9Dy0.1O3-δ in Oxidizing Atmospheres. *Solid State Ionics* **2019**. https://doi.org/10.1016/j.ssi.2018.12.006.

(38) Rothschild, A.; Menesklou, W.; Tuller, H. L.; Ivers-Tiffée, E. Electronic Structure, Defect Chemistry, and Transport Properties of SrTi 1-XFe XO 3-y Solid Solutions. *Chem. Mater.* **2006**. https://doi.org/10.1021/cm052803x.

(39) Da Silva, L. F.; M'Peko, J. C.; Andrés, J.; Beltrán, A.; Gracia, L.; Bernardi, M. I. B.; Mesquita, A.; Antonelli, E.; Moreira, M. L.; Mastelaro, V. R. Insight into the Effects of Fe Addition on the Local Structure and Electronic Properties of SrTiO3. *J. Phys. Chem. C* **2014**. https://doi.org/10.1021/jp408839q.

(40) Kresse, G.; Hafner, J. Ab Initio Molecular Dynamics for Liquid Metals. *Phys. Rev. B* **1993**. https://doi.org/10.1103/PhysRevB.47.558.

(41) Kresse, G.; Hafner, J. Ab Initio Molecular-Dynamics Simulation of the Liquid-Metalamorphous- Semiconductor Transition in Germanium. *Phys. Rev. B* **1994**. https://doi.org/10.1103/PhysRevB.49.14251.

(42) Kresse, G.; Furthmüller, J. Efficient Iterative Schemes for Ab Initio Total-Energy Calculations Using a Plane-Wave Basis Set. *Phys. Rev. B - Condens. Matter Mater. Phys.* **1996**. https://doi.org/10.1103/PhysRevB.54.11169.

(43) Kresse, G.; Furthmüller, J. Efficiency of Ab-Initio Total Energy Calculations for Metals and Semiconductors Using a Plane-Wave Basis Set. *Comput. Mater. Sci.* **1996**. https://doi.org/10.1016/0927-0256(96)00008-0.

(44) Blöchl, P. E. Projector Augmented-Wave Method. *Phys. Rev. B* **1994**. https://doi.org/10.1103/PhysRevB.50.17953.

(45) Kresse G.a Joubert, D. . From Ultrasoft Pseudopotentials to the Projector Augmented-Wave Method. *Phys. Rev. B - Condens. Matter Mater. Phys.* **1999**.

(46) Perdew, J. P.; Burke, K.; Ernzerhof, M. Generalized Gradient Approximation Made Simple. *Phys. Rev. Lett.* **1996**. https://doi.org/10.1103/PhysRevLett.77.3865.

(47) Rosov, N.; Lynn, J. W.; Lin, Q.; Cao, G.; O'Reilly, J. W.; Pernambuco-Wise, P.; Crow, J. E. Antiferromagnetic Ordering of BaPrO3 via Neutron Diffraction. *Phys. Rev. B* **1992**. https://doi.org/10.1103/PhysRevB.45.982.

(48) Anisimov, V. I.; Zaanen, J.; Andersen, O. K. Band Theory and Mott Insulators: Hubbard U Instead of Stoner I. *Phys. Rev. B* **1991**. https://doi.org/10.1103/PhysRevB.44.943.

(49) Anisimov, V. I.; Aryasetiawan, F.; Lichtenstein, A. I. First-Principles Calculations of the Electronic Structure and Spectra of Strongly Correlated Systems: The LDA + U Method. *Journal of Physics Condensed Matter*. 1997. https://doi.org/10.1088/0953-8984/9/4/002.

(50) Dudarev, S.; Botton, G. Electron-Energy-Loss Spectra and the Structural Stability of

Nickel Oxide: An LSDA+U Study. *Phys. Rev. B - Condens. Matter Mater. Phys.* **1998**. https://doi.org/10.1103/PhysRevB.57.1505.

(51) Lu, D.; Liu, P. Rationalization of the Hubbard U Parameter in CeOx from First Principles: Unveiling the Role of Local Structure in Screening. *J. Chem. Phys.* **2014**. https://doi.org/10.1063/1.4865831.

(52) Fabris, S.; De Gironcoli, S.; Baroni, S.; Vicario, G.; Balducci, G. Taming Multiple Valency with Density Functionals: A Case Study of Defective Ceria. *Phys. Rev. B - Condens. Matter Mater. Phys.* **2005**. https://doi.org/10.1103/PhysRevB.71.041102.

(53) Wang, L.; Maxisch, T.; Ceder, G. Oxidation Energies of Transition Metal Oxides within the GGA+U Framework. *Phys. Rev. B - Condens. Matter Mater. Phys.* **2006**. https://doi.org/10.1103/PhysRevB.73.195107.

(54) Andersson, D. A.; Simak, S. I.; Johansson, B.; Abrikosov, I. A.; Skorodumova, N. V. Modeling of CeO2, Ce2O3, and CeO2-x in the LDA+U Formalism. *Phys. Rev. B - Condens. Matter Mater. Phys.* **2007**, *75* (3), 035109.

(55) Momma, K.; Izumi, F. VESTA: A Three-Dimensional Visualization System for Electronic and Structural Analysis. *J. Appl. Crystallogr.* **2008**. https://doi.org/10.1107/S0021889808012016.

(56) Dronskowski, R.; Bloechl, P. E. Crystal Orbital Hamilton Populations (COHP): Energy-Resolved Visualization of Chemical Bonding in Solids Based on Density-Functional Calculations. *J. Phys. Chem.* **2002**, *97* (33), 8617–8624. https://doi.org/10.1021/J100135A014.

(57) Deringer, V. L.; Tchougréeff, A. L.; Dronskowski, R. Crystal Orbital Hamilton Population (COHP) Analysis As Projected from Plane-Wave Basis Sets. *J. Phys. Chem. A* **2011**, *115* (21), 5461–5466. https://doi.org/10.1021/JP202489S.

(58) Nelson, R.; Ertural, C.; George, J.; Deringer, V. L.; Hautier, G.; Dronskowski, R. LOBSTER: Local Orbital Projections, Atomic Charges, and Chemical-Bonding

Analysis from Projector-Augmented-Wave-Based Density-Functional Theory. *J. Comput. Chem.* **2020**, *41* (21), 1931–1940. https://doi.org/10.1002/JCC.26353.

(59) Maintz, S.; Deringer, V. L.; Tchougréeff, A. L.; Dronskowski, R. LOBSTER: A Tool to Extract Chemical Bonding from Plane-Wave Based DFT. *J. Comput. Chem.* **2016**, *37* (11), 1030–1035. https://doi.org/10.1002/JCC.24300.

(60) Maintz, S.; Deringer, V. L.; Tchougréeff, A. L.; Dronskowski, R. Analytic Projection from Plane-Wave and PAW Wavefunctions and Application to Chemical-Bonding Analysis in Solids. *J. Comput. Chem.* **2013**, *34* (29), 2557–2567. https://doi.org/10.1002/JCC.23424.

(61) Maintz, S.; Esser, M.; Dronskowski, R. EFFICIENT ROTATION OF LOCAL BASIS FUNCTIONS USING REAL SPHERICAL HARMONICS. **2016**, *47*. https://doi.org/10.5506/APhysPolB.47.1165.

(62) Kharton, V. V.; Yaremchenko, A. A.; Patrakeev, M. V.; Naumovich, E. N.; Marques, F. M. B. Thermal and Chemical Induced Expansion of La0.3Sr0.7 (Fe,Ga)O3-δ Ceramics. *J. Eur. Ceram. Soc.* **2003**, *23* (9), 1417–1426. https://doi.org/10.1016/S0955-2219(02)00308-4.

(63) Miyoshi, S.; Hong, J. O.; Yashiro, K.; Kaimai, A.; Nigara, Y.; Kawamura, K.; Kawada, T.; Mizusaki, J. Lattice Expansion upon Reduction of Perovskite-Type LaMnO3 with Oxygen-Deficit Nonstoichiometry. *Solid State Ionics* **2003**. https://doi.org/10.1016/S0167-2738(03)00281-9.

(64) Yong, A. X. B; Anderson, L. O.; Perry, N. H.; Ertekin, E. Effects of Localization and State Filling on Chemical Expansion in Doped and Undoped Praseodymium-Oxide Perovskites. *Prep.* https://doi.org/in preparation.

(65) Furuichi, S.; Tsuchiya, T.; Horiba, K.; Kobayashi, M.; Minohara, M.; Kumigashira, H.; Higuchi, T. Structural and Electrical Properties of BaPrO3-δ Thin Film with Oxygen Vacancies. *Trans. Mater. Res. Soc. Japan* **2017**, *42* (2), 15–18.

https://doi.org/10.14723/TMRSJ.42.15.

(66) Higuchi, T.; Oda, A.; Tsuchiya, T.; Suetsugu, T.; Suzuki, N.; Yamaguchi, S.; Minohara, M.; Kobayashi, M.; Horiba, K.; Kumigashira, H.; Tohru, H.; Asuka, O.; Takashi, T.; Takaaki, S.; Naoya, S.; Shohei, Y.; Makoto, M.; Masaki, K.; Koji, H.; Hiroshi, K. Hole-Ion Mixed Conduction of Orientation-Controlled BaPrO3-δ Thin Film with Mixed Valence States. *J. Phys. Soc. Japan* **2015**, *84* (11). https://doi.org/10.7566/JPSJ.84.114708.

(67) Er, D.; Li, J.; Cargnello, M.; Fornasiero, P.; Gorte, R. J.; Shenoy, V. B. A Model to Determine the Chemical Expansion in Non-Stoichiometric Oxides Based on the Elastic Force Dipole. *J. Electrochem. Soc.* **2014**. https://doi.org/10.1149/2.0101411jes.

(68) Hartley, P.; Egdell, R. G.; Zhang, K. H. L.; Hohmann, M. V.; Piper, L. F. J.; Morgan, D. J.; Scanlon, D. O.; Williamson, B. A. D.; Regoutz, A. Experimental and Theoretical Study of the Electronic Structures of Lanthanide Indium Perovskites LnInO3. *J. Phys. Chem. C* **2021**, *125* (11), 6387–6400. https://doi.org/10.1021/ACS.JPCC.0C11592.

(69) Higuchi, T.; Oda, A.; Liu, Y.-S.; Glans, P.-A.; Guo, J. Electronic Structure of $BaPr_{1-x}Yb_xO_{3-\delta}$ by Soft-X-Ray Spectroscopy. *Trans. Mater. Res. Soc. Japan* **2015**. https://doi.org/10.14723/tmrsj.40.37.

(70) Tsidilkovski, V. I.; Putilov, L. P. The Role of Deep Acceptor Levels in Hydration and Transport Processes in BaZr1 − XYxO3 – δ and Related Materials. *J. Solid State Electrochem.* **2016**. https://doi.org/10.1007/s10008-015-3087-1.

(71) Lindman, A.; Erhart, P.; Wahnström, G. Implications of the Band Gap Problem on Oxidation and Hydration in Acceptor-Doped Barium Zirconate. *Phys. Rev. B - Condens. Matter Mater. Phys.* **2015**. https://doi.org/10.1103/PhysRevB.91.245114.

(72) Tuller, H. L.; Nowick, A. S. Small Polaron Electron Transport in Reduced CeO2 Single Crystals. *J. Phys. Chem. Solids* **1977**. https://doi.org/10.1016/0022-3697(77)90124-X.

(73) De Souza, R. A.; Metlenko, V.; Park, D.; Weirich, T. E. Behavior of Oxygen

Vacancies in Single-Crystal SrTiO 3: Equilibrium Distribution and Diffusion Kinetics. *Phys. Rev. B - Condens. Matter Mater. Phys.* **2012**. https://doi.org/10.1103/PhysRevB.85.174109.

(74) Nagaraja, A. R.; Perry, N. H.; Mason, T. O.; Tang, Y.; Grayson, M.; Paudel, T. R.; Lany, S.; Zunger, A. Band or Polaron: The Hole Conduction Mechanism in the p-Type Spinel Rh 2ZnO 4. *J. Am. Ceram. Soc.* **2012**. https://doi.org/10.1111/j.1551-2916.2011.04771.x.

(75) Schrade, M.; Magrasó, A.; Galeckas, A.; Finstad, T. G.; Norby, T. The Band Gap of BaPrO3 Studied by Optical and Electrical Methods. *J. Am. Ceram. Soc.* **2016**. https://doi.org/10.1111/jace.13961.

(76) Sakhya, A. P.; Rai, D. P.; Sandeep; Dutta, A.; Thapa, R. K.; Sinha, T. P. Electronic, Optical and Thermoelectric Properties of PrMO3 (M = Al, Ga, In) from First-Principles Calculations. *RSC Adv.* **2016**. https://doi.org/10.1039/c6ra08875a.

(77) Kim, C. S.; Bishop, S. R.; Perry, N. H.; Tuller, H. L. Electro-Chemo-Mechanical Studies of Perovskite-Structured Mixed Ionic-Electronic Conducting SrSn1-XFexO3-x/2+δpart I: Defect Chemistry. *J. Electroceramics* **2017**. https://doi.org/10.1007/s10832-017-0064-3.

(78) Chen, X.; Grande, T. Anisotropic Chemical Expansion of La1-XSrxCoO 3-δ. *Chem. Mater.* **2013**. https://doi.org/10.1021/cm304040p.

(79) Bishop, S. R.; Tuller, H. L.; Kuru, Y.; Yildiz, B. Chemical Expansion of Nonstoichiometric Pr0.1Ce0.9O2-δ: Correlation with Defect Equilibrium Model. *J. Eur. Ceram. Soc.* **2011**. https://doi.org/10.1016/j.jeurceramsoc.2011.05.034.

(80) Marrocchelli, D.; Bishop, S. R.; Tuller, H. L.; Yildiz, B. Understanding Chemical Expansion in Non-Stoichiometric Oxides: Ceria and Zirconia Case Studies. *Adv. Funct. Mater.* **2012**. https://doi.org/10.1002/adfm.201102648.

(81) Perry, N. H.; Marrocchelli, D.; Bishop, S. R.; Tuller, H. L. (Invited) Understanding and

Controlling Chemo-Mechanical Coupling in Perovskite Oxides. *ECS Trans.* **2016**. https://doi.org/10.1149/07224.0001ecst.

(82) Bishop, S. R.; Duncan, K. L.; Wachsman, E. D. Defect Equilibria and Chemical Expansion in Non-Stoichiometric Undoped and Gadolinium-Doped Cerium Oxide. *Electrochim. Acta* **2009**. https://doi.org/10.1016/j.electacta.2008.09.026.

(83) Thimsen, E.; Biswas, S.; Lo, C. S.; Biswas, P. Predicting the Band Structure of Mixed Transition Metal Oxides: Theory and Experiment. *J. Phys. Chem. C* **2009**. https://doi.org/10.1021/jp807579h.

(84) Deml, A. M.; Stevanović, V.; Holder, A. M.; Sanders, M.; Ohayre, R.; Musgrave, C. B. Tunable Oxygen Vacancy Formation Energetics in the Complex Perovskite Oxide SrxLa1-XMnyAl1- YO3. *Chem. Mater.* **2014**. https://doi.org/10.1021/cm5033755.

(85) Hwang, J.; Feng, Z.; Charles, N.; Wang, X. R.; Lee, D.; Stoerzinger, K. A.; Muy, S.; Rao, R. R.; Lee, D.; Jacobs, R.; Morgan, D.; Shao-Horn, Y. Tuning Perovskite Oxides by Strain: Electronic Structure, Properties, and Functions in (Electro)Catalysis and Ferroelectricity. *Materials Today*. 2019. https://doi.org/10.1016/j.mattod.2019.03.014.

(86) Akhade, S. A.; Kitchin, J. R. Effects of Strain, d-Band Filling, and Oxidation State on the Surface Electronic Structure and Reactivity of 3d Perovskite Surfaces. *J. Chem. Phys.* **2012**. https://doi.org/10.1063/1.4746117.

(87) Zimmermann, R.; Steiner, P.; Claessen, R.; Reinert, F.; Hüfner, S.; Blaha, P.; Dufek, P. Electronic Structure of 3d-Transition-Metal Oxides: On-Site Coulomb Repulsion versus Covalency. *J. Phys. Condens. Matter* **1999**. https://doi.org/10.1088/0953-8984/11/7/002.

(88) Suntivich, J.; May, K. J.; Gasteiger, H. A.; Goodenough, J. B.; Shao-Horn, Y. A Perovskite Oxide Optimized for Oxygen Evolution Catalysis from Molecular Orbital Principles. *Science (80-.).* **2011**. https://doi.org/10.1126/science.1212858.

(89) Hu, Z.; Kaindl, G.; Ogasawara, H.; Kotani, A.; Felner, I. Ln-4f/Ligand-2p Covalence in

BaLnO3 and Cs3LnF7 (Ln=Ce, Pr, Tb). *Chem. Phys. Lett.* **2000**.

https://doi.org/10.1016/S0009-2614(00)00656-4.

(90) Cammarata, A.; Rondinelli, J. M. Covalent Dependence of Octahedral Rotations in Orthorhombic Perovskite Oxides. *J. Chem. Phys.* **2014**.

https://doi.org/10.1063/1.4895967.

For Table of Contents Only

Optimizing the stability and lifetime of mixed ionic and electronic conductors (MIECs) and devices requires addressing their redox-induced strain. We provide insight into this chemo-mechanical coupling by demonstrating that redox on oxygen, rather than on a multivalent cation, results in the lowest coefficients of chemical expansion measured for perovskite oxides, providing a novel method for reducing chemical strain in MIECs.